



Fabrication, characterization and analysis of a prototype high purity germanium detector for ^{76}Ge -based neutrinoless double beta decay experiments

A. Jany¹, M. Misiaszek¹, T. Mroz¹, K. Panas^{1,a} , G. Zuzel¹, M. Wojcik¹, K. Brudecki², J. Jurkowski², J. W. Mietelski², R. Misiak², M. Marszałek², M. Mitura-Nowak²

¹ Institute of Physics, Jagiellonian University, 30-348 Kraków, Poland

² Institute of Nuclear Physics Polish Academy of Sciences, 31-342 Kraków, Poland

Received: 23 February 2020 / Accepted: 21 December 2020
© The Author(s) 2021

Abstract Experiments searching for the neutrinoless double beta decay in ^{76}Ge are currently achieving the lowest background level and, in connection with the excellent energy resolution of germanium detectors, they exhibit the best discovery potential for the decay. Expansion to a ton scale of the active target mass is presently considered – in this case on-site production of the detectors may be an option. In this paper we describe the fabrication and characterization procedures of a prototype detector with a small p^+ contact, which enhances the abilities of the pulse shape discrimination – one of the most important tools for background reduction. Simulations of the shapes of pulses from the detector were carried out and tuned, taking the advantage of the fact that all the parameters of the Ge crystal, cryostat and of the spectroscopic chain were known. As a result, the pulse shape analyses performed on the simulated and measured data agree very well. The worked out method allows to optimize geometry and crystal parameters in terms of pulse shape analysis efficiency, before the actual production of the detectors.

1 Introduction

Since the first calculations of the neutrinoless double beta ($0\nu\beta\beta$) decay rates by Maria Goeppert-Mayer in 1935 [1] the process was sought as a proof of the Majorana nature of neutrinos, as proposed by Furry in 1939 [2]. There are 35 isotopes, for which single beta decay is energetically forbidden, however double beta decay can theoretically take place [3]. ^{76}Ge is one of these isotopes.

The $0\nu\beta\beta$ process is very rare and therefore its observation requires a setup of very low background, i.e., all other sources of ionizing radiation have to be eliminated.

The high purity germanium (HPGe) detectors are fabricated from Ge monocrystals, which are very radiopure (have practically negligible content of radioactive isotopes) and can be enriched in ^{76}Ge [4]. Furthermore, they offer an excellent energy resolution. Thus, the $0\nu\beta\beta$ decay experiments applying germanium may achieve ultra-low background, very good separation between the $2\nu\beta\beta$ and $0\nu\beta\beta$ decay energy spectra and high detection efficiency (detector \equiv source).

Past experiments, like the Heidelberg-Moscow (HDM) [5] and the International Germanium Experiment (IGEX) [6] provided for a long time the best limits for the half-life of the $0\nu\beta\beta$ process ($T_{1/2}^{0\nu}$). The GERMANIUM DETECTOR ARRAY (GERDA) [7] is a project based on ^{76}Ge as well. In 2013 GERDA obtained the limit of $T_{1/2}^{0\nu} \geq 2.1 \times 10^{25} \text{ yr}$ [8], and refuted with 99 % probability the claim of the $0\nu\beta\beta$ decay observation [9]. In Phase II of GERDA [10–14] the lowest background in the field of $5.2 \times 10^{-4} \text{ cts/(keV}\cdot\text{kg}\cdot\text{yr)}$ has been reached. After combining all available data (Phase I + Phase II) and applying the frequentist analysis the lowest limit for $T_{1/2}^{0\nu}$ of $1.8 \times 10^{26} \text{ yr}$ at 90% C.L. has been set. The limit coincides with the sensitivity, defined as the median expectation under no signal hypothesis. By assuming in the Bayesian framework a priori equiprobable Majorana neutrino masses instead of equiprobable signal strengths one gets a stronger limit of $2.3 \times 10^{26} \text{ yr}$ (90% C.L.) [14].

Basing on the technology and expertise from GERDA and MAJORANA, the LEGEND experiment is planned. Its first phase, LEGEND-200 (200 kg of ^{76}Ge) [15], is presently under preparation. LEGEND-200 will use the GERDA infrastructure and it will allow to push the limit for the $0\nu\beta\beta$ decay half-life into the range of 10^{27} yr . Ultimately, LEGEND-1000 (1 ton of ^{76}Ge) shall be able to provide the limit for $T_{1/2}^{0\nu}$ at the level of 10^{28} yr [16].

^a e-mail: panas.krzysztof@gmail.com (corresponding author)

Anticipated improvement of the experiment's sensitivity requires not only an increase of the target mass, but also further reduction of the background at $Q_{\beta\beta}$, while preserving very good energy resolution of the germanium detectors. Comparing to GERDA Phase II, in LEGEND-1000 the background index needs to be pushed down by a factor 50 to reach the 10^{-5} cts/(keV·kg·yr) level.

The increase of the target mass may be achieved by deployment of an appropriate number of detectors made from enriched Ge (^{enr}Ge). However, the small BEGe-type (Broad Energy Germanium) detectors [17] used in GERDA Phase II may not be an optimal choice because, with their average mass of about 0.7 kg, one would need more than 1300 read-out channels (large number of electronic components, which may constitute a potential background source). On the other hand, classical semi-coaxial detectors (masses up to ~ 2.7 kg) show much poorer pulse shape analysis (PSA) abilities [18–21]. Recently developed the so-called Inverted Coaxial (IC) detectors, which offer larger mass and the BEGe-like PSA performance [22, 23], thus they are considered to be applied in LEGEND-200. In GERDA Phase II a significant fraction of background came from the surface events [12] caused by the decays of ^{210}Po (partly supported by ^{210}Pb). ^{210}Po is a long-lived ^{222}Rn daughter and could be deposited on the detector surfaces during their production or handling. The identification of ^{210}Po decays via PSA is thus crucial.

Another unsolved problem is the radiopurity of Li, which is used to form the thick (~ 0.7 mm), outer n^+ contact. Typically, it is formed by immersing the HPGe crystal in a bath containing Li (e.g. molten $\text{LiNO}_3\text{--KNO}_3$ eutectic [24]), which at elevated temperature diffuses into Ge. The process takes several hours and may result in a residual contamination of the detector e.g. with ^{40}K present in the bath.

In LEGEND-1000 large-scale detector production and further reduction of the background will be crucial tasks to achieve needed sensitivity. The best way to achieve these goals may be on-site (underground) production of the germanium detectors under fully controlled conditions, e.g. in a ^{222}Rn -free atmosphere [25]. This would also solve the problem of the cosmogenic activation of the detectors if the manufacturing process takes place on the surface. Besides crystal pulling, the transformation of the HPGe crystal into a working detector is the most delicate part of the whole production process. Possession of this technology would allow not only for fabrication, but also for on-site repair of the existing detectors avoiding their transportation and related risks of contamination (e.g. activation).

In the first part of this paper we describe the manufacturing process of a prototype of a p-type HPGe detector, formation of a p-n junction by lithium thermodiffusion and boron implantation. After the successful production the detector was characterized by measuring its leakage current, capacitance and the energy resolution at a wide range of bias volt-

ages. The measurements were confronted with the various models predicting the capacitance and the depletion voltage. Using the crystal parameters supplied by the manufacturer we found a very good agreement between the measurements and the simulation.

In the second part of the paper we discuss the efficiency of a PSA method developed by our group [20] and applied to the prototype. It is compared with analysis based on simulated signals. The latter were calculated using energy depositions by ^{228}Th and ^{56}Co and simulated electric field in the detector. The detector model has been optimized taking the advantage of the fact that the parameters of the crystal (dimensions, level of impurities), the geometry of the cryostat and the response of the preamplifier were known. As a result, the analyses performed for the measured and simulated pulses agree very well. Moreover, we show that the PSA trained on the simulated pulses may be applied to the real data and vice versa. A well-understood model of the HPGe detectors will make possible studies of the optimal configuration with respect to the crystal/electrodes size/geometry, maximizing the PSA performance. The model can be also used to evaluate systematic uncertainties of the PSA methods applied to larger detectors, where e.g. distribution of calibration events form double escape peak(s) (used as proxies for the signal in the PSA training) is inhomogeneous.

Application of various sources to verify the separation efficiencies of PSA gives a unique opportunity to estimate the systematic uncertainties of the analysis and investigate effects related to potential energy dependence of the cut. In our case we used events from a ^{228}Th source to train/calibrate the analysis method and then the cut was applied to ^{56}Co events. A very good agreement of survival fractions of similar types of events has been achieved. For the ^{56}Co events from the full energy peaks between 1175.1 keV and 2598.5 keV a slight energy dependence has been noticed (acceptances of 23.9% and 20.3%, respectively). This showed up also for the simulated pulses, but the effect was weaker.

Our pulse shape analysis based on the artificial neural network was also compared with the widely used A/E method [18, 19, 21]. For the prototype the neural network provided better results, however for bigger detectors the difference may not be that significant. A clear advantage, as it will be shown, of our approach is the “ability” of the network to clearly separate background and signal events (two clear bands) what results in relatively easy definition of the cut value (even if there is a slight energy dependence). Moreover, the cut is stable providing constant survival probabilities for wide range of its parameter values.

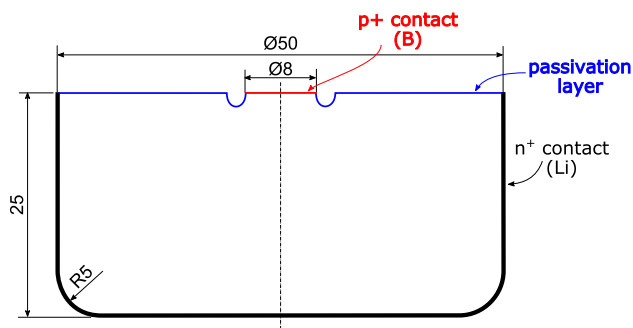


Fig. 1 Scheme of the manufactured prototype detector. The thick black line represents the n^+ contact created by the lithium thermodiffusion. The red and blue lines represent the p^+ electrode implanted with boron and the passivated surface, respectively. Dimensions are given in mm

2 Fabrication of the detector

The described detector of the p-type was manufactured in the so-called “small-anode” geometry [26], which minimizes the terminal electrical capacitance of the diode. It can be approximated using a hemispherical capacitor model, with the second (larger) electrode moved to infinity:

$$C = 2\pi\epsilon\epsilon_0r_0 \quad (1)$$

where: ϵ is the dielectric constant of germanium, ϵ_0 is the vacuum permittivity and r_0 is the radius of the readout electrode, a parameter which may be optimized for achieving the lowest possible capacitance, but with the electric field allowing for the good charge collection.

As a consequence of the small capacitance the noise is reduced, what allows to achieve very good energy resolution, as well as a low energy detection threshold [27]. The latter is especially important for detection of events with small energy depositions, like those caused by interactions of dark matter particles or neutrinos (coherent neutrino scatterings on Ge nuclei). The downside of the small anode geometry is that the resulting electric field in the detector volume can be too weak in some regions to effectively drift created charges. This can lead to trapping effects and finally to amplitude deficit of the registered pulses. Areas near the edges of the crystal (far from the readout electrode) are of a special concern – the electric field is weak there and depends mostly on the concentration of impurities in the crystal [27]. In order to avoid these problems the lower edge of the prototype detector was rounded (see Fig. 1) to effectively remove the weak field regions.

We started with a cylindrical p-type HPGe monocrystal with the dimensions of 50.4 mm in diameter and 25.3 mm in height. The material was supplied by Umicore company [28] and had very low impurity concentration, which was measured by the manufacturer to be $0.58 \times 10^{10} \text{ cm}^{-3}$ and $0.48 \times 10^{10} \text{ cm}^{-3}$ at the top and at the bottom planes,

respectively. The first step in the fabrication process was the mechanical lapping and grinding of the crystal, which reduced the dimensions to 50 mm and 25 mm, respectively (as shown in Fig. 1). To fabricate the electrical contacts of the detector we followed the technique developed in the Institute of Nuclear Physics, Polish Academy of Sciences (IFJ PAN) in Krakow [29]. The n^+ electrode was created by lithium evaporation and thermodiffusion in a vacuum chamber. This effectively creates the p- n^+ junction, which under the large reverse bias depletes the whole volume of the crystal – this is where the effective radiation detection takes place. Appropriate amount of Li evaporated in dedicated cells was released when the crystal reached 300 °C. High temperature helps Li deposited on the surface to diffuse into the germanium. After evaporation the crystal was left to cool down for about 1 hour while still in vacuum and then the system was vented to reach room temperature. To obtain a clean surface and good electrical contact the crystal was then etched in the 3:1 $\text{HNO}_3:\text{HF}$ mixture to remove an excess of lithium. As shown in Fig. 1 the Li-diffused layer was formed on the bottom and on the side surfaces of the crystal.

After Li evaporation the next step was to drill a groove with the internal diameter of 8 mm and depth of ca. 2 mm. Usually the passivated groove separates the n^+ electrode, where bias voltage is applied, from the p^+ contact used for signal readout. If the entire upper surface is going to be passivated (as in our case), the groove is not necessary, but it helps to mask the p^+ contact with an acid-resistant tape during the etching of the crystal.

The p^+ electrode was created by boron implantation [30], which creates good electron blocking contacts [31]. The implantation was performed with ions of two energies: 25 and 17 keV, with doses of 10^{13} and 10^{14} ions/ cm^2 , respectively.

In the last step of the fabrication process a passivation layer was formed on the detector top surface. This was performed by masking the p^+ and n^+ contacts with an acid-resistant tape, etching the surface and quenching the etchant with methanol [32]. After drying with nitrogen gas the detector was mounted in a dedicated holder and installed with the front-end (FE) electronics in a vacuum cryostat. Another passivation technique we have tested was based on chemically grown GeO_2 layer. It turned out to be much more robust and resistant to the atmospheric conditions. More systematic studies of that technology is planned as we think it has potential to replace in some situations the widely used sputtering technique.

3 Characterization of the detector

The detector’s preamplifier was equipped with a low noise J-FET (junction field-effect transistor, type 2N4393), which

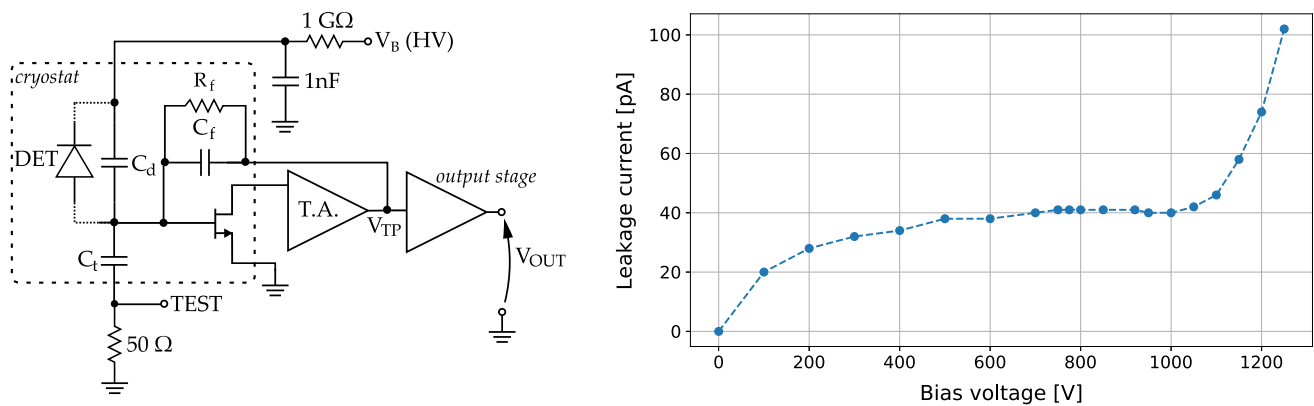


Fig. 2 Left panel: schematic of the preamplifier circuit. The test point voltage (V_{TP}) was used to determine the leakage current (see the text for the explanation). Right panel: leakage current of the fabricated detector as a function of the bias voltage. The operating voltage was set to 1100 V

was mounted on the detector holder in the vacuum cryostat (temperature near 77 K during normal operation). The used preamplifier was of a resistive feedback type, therefore, a feedback resistor and a capacitor (in Fig. 2 denoted as R_f and C_f , respectively) were also mounted inside the cryostat (close to the J-FET's gate). The same electronic setup was used earlier with a small (10% relative efficiency, capacitance C_d of about 20 pF) commercial semi-coaxial p-type detector providing the energy resolution (defined as the full width at half of the maximum: FWHM) of 1.8 keV for the 1332.5 keV ^{60}Co γ line. Therefore, we expected similar performance assuming that other detector parameters (like leakage current or charge collection) will be within the expected regimes. It should be underlined that the described configuration was not optimal due to the relatively high gate capacitance of the 2N4393 J-FET (≈ 14 pF [33]) compared to the expected capacitance of the detector (≈ 3.5 pF – see Eq. 1).

The first determined characteristic was the so-called current–voltage (I–V) curve. It represents the leakage current of the detector as a function of the bias voltage. The current was not measured directly with a picoammeter but it was deduced from the test point voltage, i.e., DC voltage observed at the output of the first stage of the preamplifier (V_{TP} in Fig. 2) while slowly increasing the bias voltage V_B . Since the J-FET's gate has very high impedance, the leakage current is forced to flow through the feedback resistor R_f . This additional current creates a potential drop on R_f , what lowers the value of V_{TP} . By comparing the test point voltage with- and without the bias ($V_{TP\text{ OFF}}$ and $V_{TP}(V_B)$, respectively), the leakage current can be approximated by the following equation:

$$I_{\text{leak}}(V_B) = \frac{|V_{TP\text{ OFF}} - V_{TP}(V_B)|}{R_f} \quad (2)$$

The obtained I–V curve is plotted in the right panel of Fig. 2. A sharp increase of the leakage current has been

noticed above 1100 V, therefore, this bias voltage has been chosen as the operational voltage of the detector.

Next, a spectral voltage scan was performed – using a calibration source several spectra were recorded for a set of bias voltages. For each V_B value the centroid and the full width at the half maximum of the 1332.5 keV ^{60}Co peak were extracted by fitting an appropriate Gaussian function. The background under the peak was included in the fit by adding a first order polynomial. The best achieved FWHM was equal to 1.90 keV at 1000 V – see Fig. 3. The operating voltage was set to 1100 V to strengthen the electric field and alleviate a possible problem related to the charge trapping (for 1100 V the energy resolution was measured to be 1.96 keV, which is insignificantly worse compared to the optimal value). The centroid of the 1332.5 keV ^{60}Co peak did not change any more above 800 V, which is the indication that the detector achieves a full depletion near this voltage.

To measure the capacitance–voltage (C–V) curve we applied the method described in [34]. Its advantage is that it does not require a removal of the input J-FET for the measurement. Therefore, the detector can operate in almost unchanged conditions and acquire energy spectra as usual. On the other hand, the standard C–V curve measurement method needs to access both electrodes of the detector, which would require disconnection of the input J-FET inside the cryostat.

In a standard spectroscopic configuration the test signal is provided through the test capacitance C_t (see Fig. 4a). To measure the detector capacitance test pulses were instead fed through an additional voltage divider (gain of 0.2, total resistance of 50 Ω) connected to the voltage filter capacitor (see Fig. 4b). In principle the test capacitor C_t can be left floating after disconnecting the test signal, but in our measurements we removed it to reduce the parasitic capacitance at the J-FET gate node.

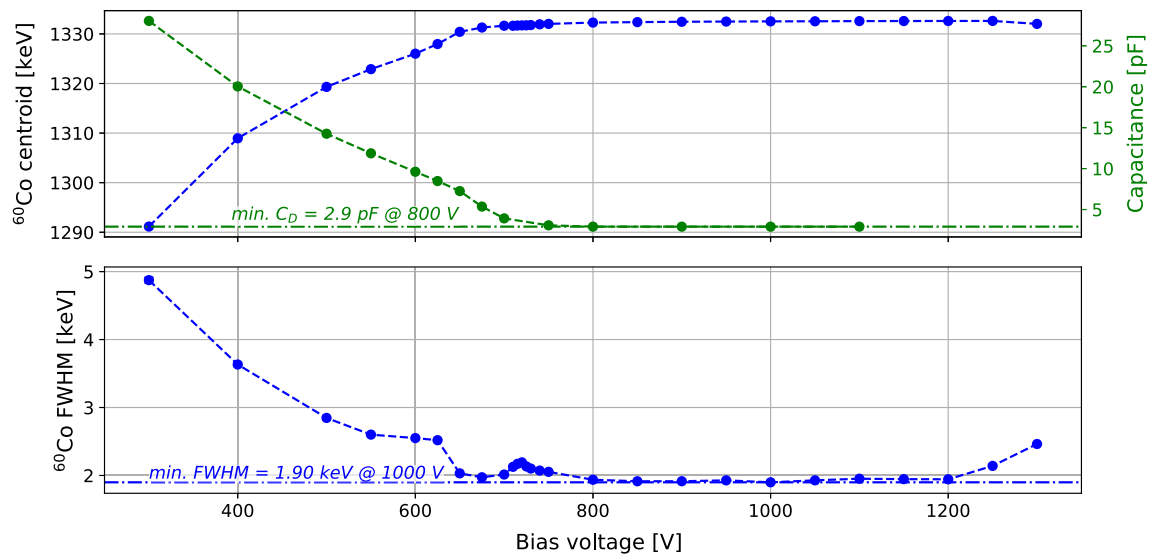


Fig. 3 Voltage scan of the prototype detector. The upper panel shows the centroid of the 1332.5 keV ^{60}Co peak. It stopped changing its position above 750 V – the value is closely correlated with the depletion voltage determined from the C–V curve (upper panel, green curve).

The bottom panel shows the energy resolution as a function of the bias voltage. The resolution was defined as the full width at half of the 1332.5 keV ^{60}Co peak maximum (FWHM)

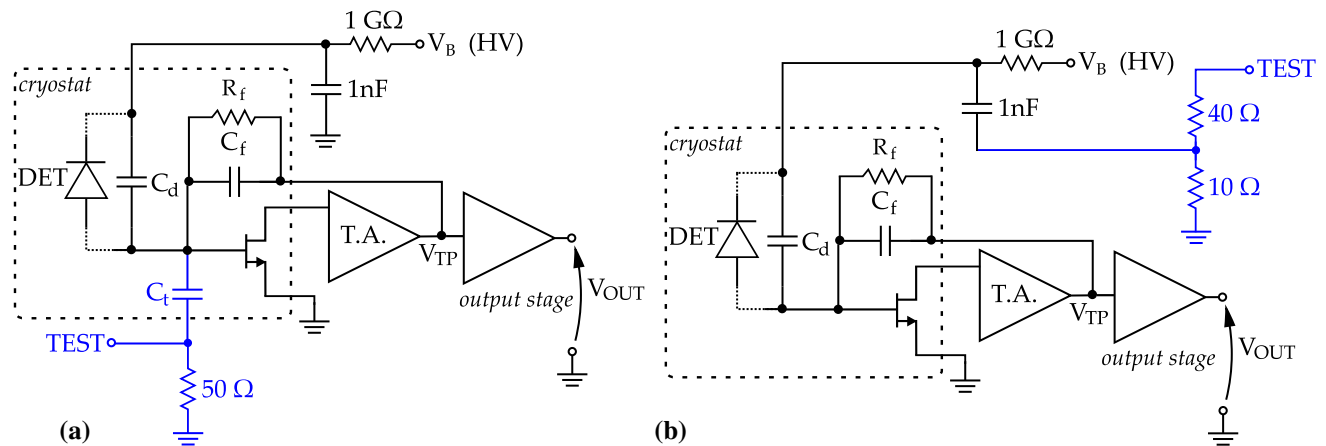


Fig. 4 Left panel **a**: Standard charge sensitive preamplifier configuration with the test pulser (in blue) – the signal is fed through a test capacitance C_t placed inside the cryostat, close to the input J-FET. Right panel **b**: Modified test pulser setup for the capacitance measurement. Instead of being fed through the test capacitance C_t , the pulser signal is injected

through the high voltage filter capacitor and then through the detector capacitance. Since the filter capacitance is much larger than the detector capacitance and they are connected in series, the signal amplitude is mostly determined by the detector capacitance (C_d), which changes with the applied bias voltage

The amplitude of the pulse at the preamplifier's output depends on the detector capacitance C_d as follows:

$$Q_{in} = V_{test} C_d \quad V_{out} = \frac{Q_{in}}{C_f} \quad (3)$$

The bias voltage of the detector was varied and pulse height spectra were recorded using a typical readout chain based on a shaping amplifier and a multichannel analyzer (MCA). Afterwards, the centroid of the pulser peak was derived from the obtained spectra. However, at this point the

centroid is expressed either in a channel number or energy units. To relate the centroid of the pulser peak with capacitance we irradiated the detector with a ^{137}Cs source for the bias voltage of 1100 V. From the previous measurement of ^{60}Co centroid, we know that for this voltage the peak position is stable and therefore we collect the full charge produced in the interactions. The created charge by the γ -ray corresponding to the full energy peak is equal to:

$$Q_\gamma = e \frac{E_\gamma}{\epsilon} \quad (4)$$

where E_γ is the energy of the γ -ray (in this case 662 keV), ϵ is the energy needed to create a single electron-hole pair in germanium ($\epsilon = 2.975$ eV) and e is the elemental charge. After calibrating the spectrum, we could calculate Q_{in} (and therefore C_d) from a simple proportion between the pulser and the ^{137}Cs full energy peak centroids.

The result of the capacitance measurement is plotted in Fig. 3 (green curve). The terminal capacitance (at full depletion) is achieved at 800 V and is equal to $C_D = 2.9$ pF. This shows that Eq. 1 can be used as a good rule-of-thumb approximation of the capacitance for this type of geometry, since the calculated value of 3.5 pF is close to the measured one. Also, both the C–V and centroid vs. voltage curves stabilize for a very similar bias voltage of ca. 800 V. Although small variations of the peak centroid are still visible over 800 V, this method can be used as a good approximation of the depletion voltage of the detector if the C–V measurements are not available.

Figure 5 shows the spectrum obtained by irradiating the detector (biased at $V_B = 1100$ V) by a multi isotope calibration source (mixture of various isotopes like ^{241}Am , ^{57}Co , ^{60}Co and others). The FWHM values were calculated for every peak and plotted as a function of the energy (bottom panel of Fig. 5). By fitting an analytic function, which takes into account electronics noise, charge carriers statistics and the charge collection efficiency, it is possible to determine the electronic noise level in the system. The fitted function, taken from [35] is the following:

$$\text{FWHM}(E) = 2.35\sqrt{\epsilon^2 \text{ENC}^2 + \epsilon F E + c^2 E^2} \quad (5)$$

where ENC is the equivalent noise charge expressed in electrons, F is the Fano factor for Ge, and c is a coefficient related to the charge collection. From the fit shown in the bottom panel of Fig. 5 we obtained: $\text{ENC} = 129.4 e^-$, $F = 0.12$ and $c = 1.9 \times 10^{-4}$ (both F and c are dimensionless). The Fano factor F is in agreement with the values available in the literature: 0.058–0.129 [36].

4 Pulse shape analysis

A single energy deposition in the germanium detector is often described as a single-site event (SSE) while multi-site events (MSEs) are related to several interactions. The difference between SSEs and MSEs is of primary interest for experiments like GERDA, because in the double beta decays the two electrons deposit their energies in Ge within about 1 mm^3 , thus, they may be considered as point-like events (signal). On the other hand, background events caused e.g. by multiple Compton scattered γ -rays are of the multi-site type and should be rejected. In the γ -ray spectrometry the situation is different: as the signal one considers MSEs (characteristic

for the full energy peaks used to evaluate the activities) and SSEs, like e.g. the Compton scattered γ -rays contributing to the continuum need to be rejected as background events [20].

In order to test the PSA performance of the manufactured detector pulse shapes from the preamplifier were recorded by a fast (100 MHz/16 bit) flash analog-to-digital (FADC) converter. The applied analysis method is based on the artificial neural network (ANN) trained on the MSEs (background) and on the SSEs (signal) waveforms extracted from a calibration spectrum, which was obtained by irradiating the detector with a ^{228}Th source. Different regions in the calibration spectrum may be considered as containing events, which are proxies for either SSEs or MSEs. For example, events in the double escape peak (DEP) and these from the Compton edge (CE, 2382 keV) are mostly SSEs, while those from the ^{212}Bi full energy peak (FEP), from the single escape peak (SEP) and from the region of multiple Compton scatterings (MCS, between 2400 keV and 2614.5 keV) are mostly of multi-site type. Thus, different options for training and validation of the PSA are possible. A detailed description of the applied analysis method can be found in [20] – since it was followed exactly as described, it will not be explained here.

4.1 Application of PSA to the ^{228}Th spectrum

The last disintegration in the ^{228}Th decay chain takes place in the ^{208}Tl nuclei, with the emission of 2614.5 keV γ -ray.¹ As discussed above, from the ^{228}Th spectrum we can extract events for training and verification of PSA. Preamplifier waveforms were digitized with FADC and off-line digital filtering was performed for energy reconstruction. For training of the neural network we used 9000 events from DEP (SSEs) and FEP (MSEs) at 1592.5 keV and 1620.5 keV, respectively. The cut on the neural network output value was set assuming that 90% of the DEP events should survive it. After the training phase the defined cuts were fixed and they can be applied to classify events from different regions of the ^{228}Th spectrum.

The classified events from the ^{228}Th dataset are visualized in Fig. 6. The histogram shows a 2D distribution (normalized with respect to the peak intensity, i.e., the sum of bin values in each column is equal to 1) of events with calculated classifier values as a function of the reconstructed energy. The obtained acceptance values for different peaks are collected in Table 1. The results show that the population of events in the ^{212}Bi and ^{208}Tl FEPs are reduced to 23.1% and 20.3%, respectively. For SEP we observe even more reduction – only 15.9% of events survive the cut. The effect of the PSA cut on different peaks from ^{228}Th spectrum is visualized in Fig. 7.

¹ Two decay modes are possible, $^{212}\text{Bi} \rightarrow ^{212}\text{Po} \rightarrow ^{208}\text{Pb}$ and $^{212}\text{Bi} \rightarrow ^{208}\text{Tl} \rightarrow ^{208}\text{Pb}$, with the branching ratios of 64% and 36%, respectively.

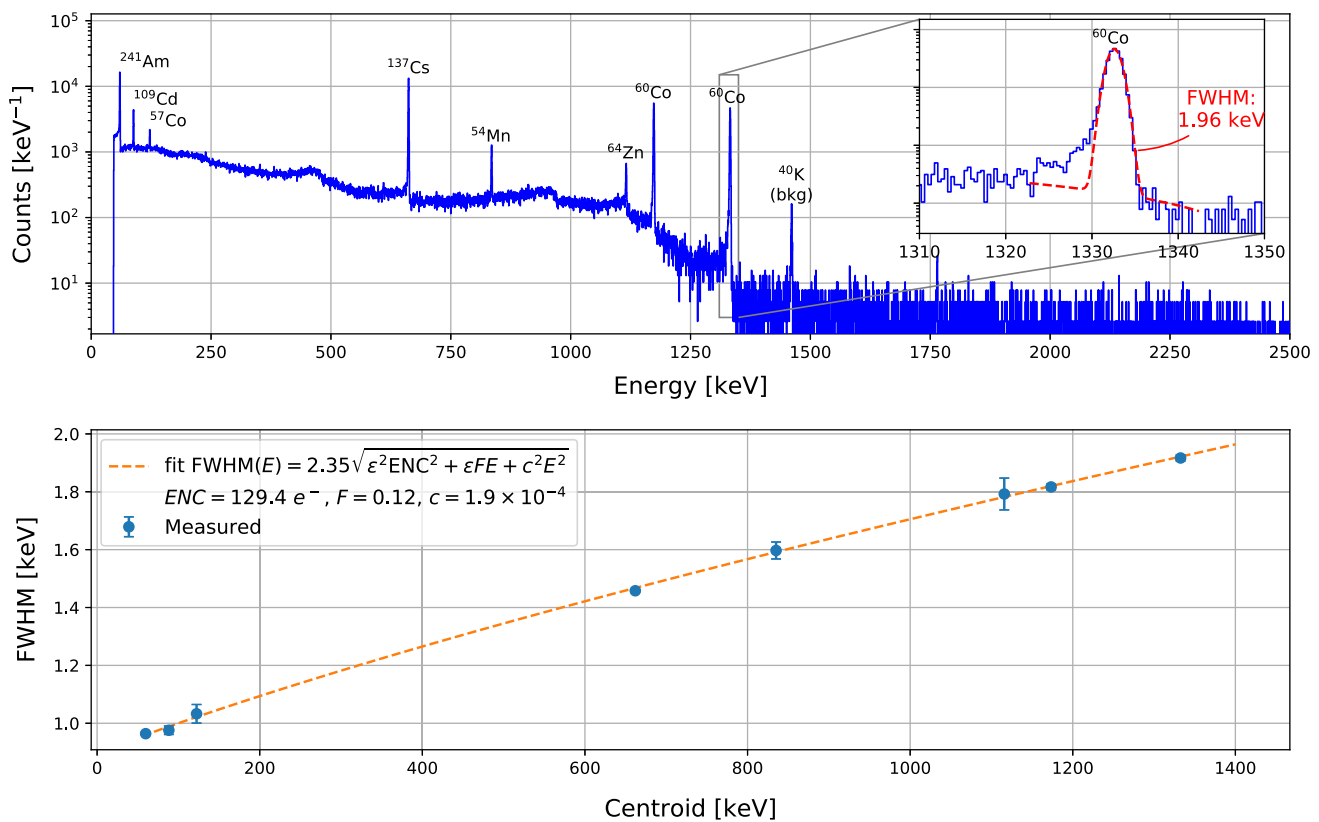


Fig. 5 Upper panel: Energy spectrum obtained by irradiating the prototype detector by a multi-isotope calibration source. Lower panel: FWHM as a function of the energy. A fit of the formula to data shown in the upper left corner is also included. It allows to determine the noise level and the Fano factor for Ge – see the text for a detailed explanation

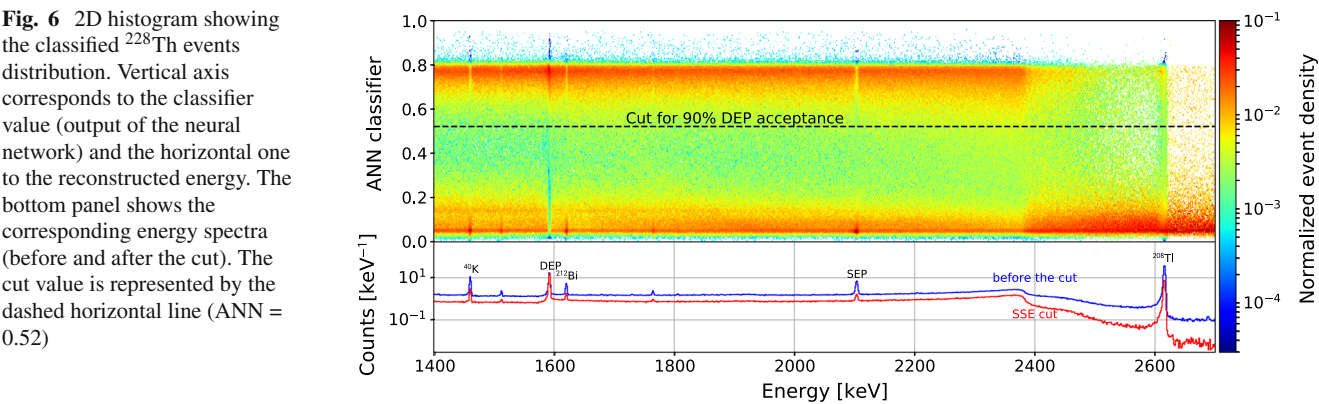


Table 1 Acceptances of events from various peaks present in the ²²⁸Th spectrum after application of PSA. The cut value on ANN output was set to preserve 90% of events form DEP, resulting in the value of 0.52. The last column contains, for comparison purposes, PSA results obtained with A/E method

Energy (keV)	Peak type	Survival prob. ANN PSA (%)	Survival prob. A/E (%)
1592.5	DEP	90.1	90.1
1620.5	²¹² Bi	22.8	30.5
2103.5	SEP	15.5	22.1
2614.5	²⁰⁸ Tl	21.0	38.0

Fig. 7 Close-up of the ^{228}Th spectrum before and after the cut rejecting MSEs (the same spectrum as in the bottom panel of Fig. 6), showing the effect of the PSA method on peaks consisting of events of different types. Suppression of MSEs in SEPs and FEPs is clearly visible, while SSEs in the DEP are mostly accepted

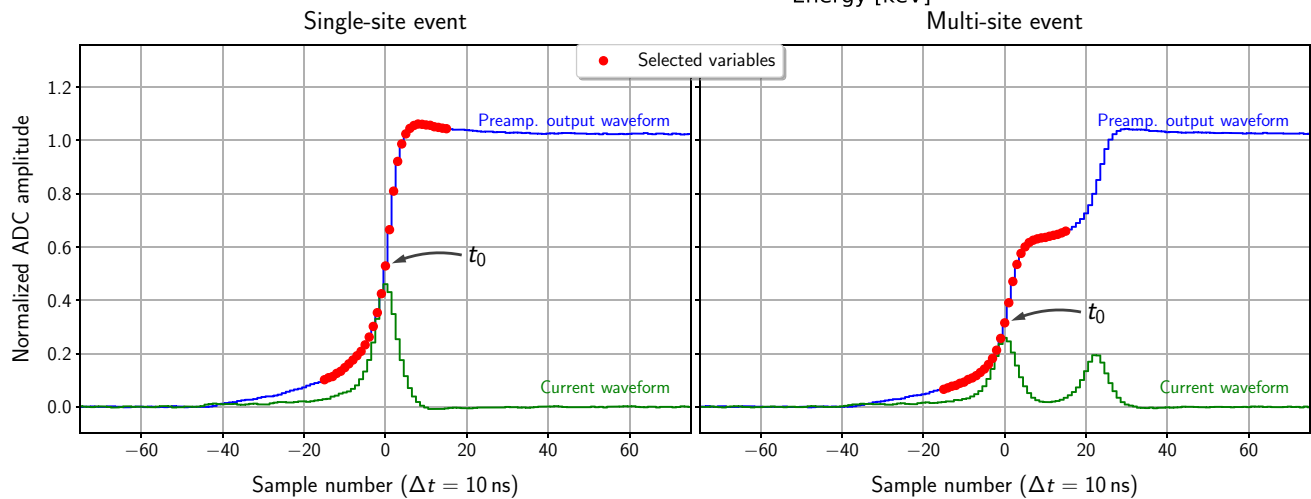
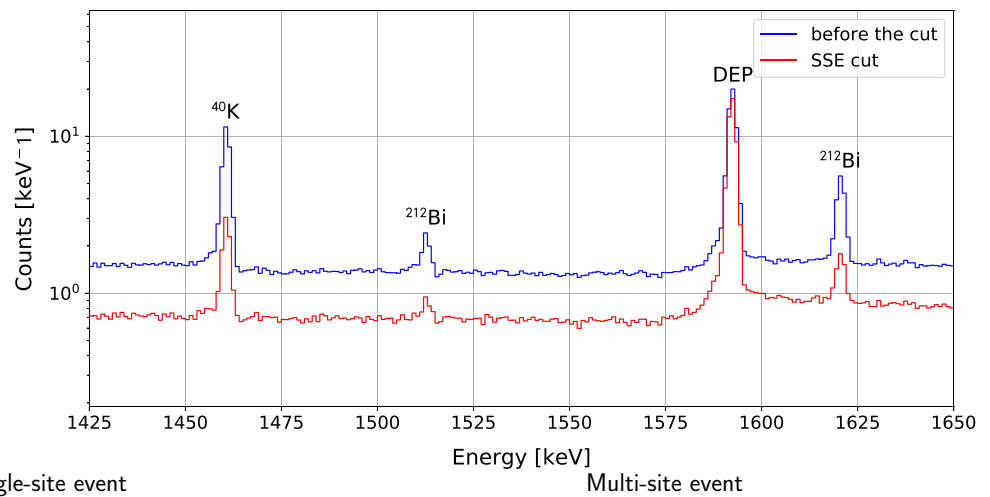


Fig. 8 Example of digitized pulses from the preamplifier (normalized with respect to the amplitude) for typical single- and multi-site events. The plot shows also corresponding current pulses (obtained by the differentiation, in green) and points (in red) selected for pulse shape analysis

For comparison purposes data from ^{228}Th dataset was also analyzed using the A/E (A over E) method [18], which was used for background reduction in GERDA [19] experiment (MAJORANA DEMONSTRATOR experiment uses a similar method – AvSE [21]). In this method a ratio of current and charge pulses is calculated – single-site events have higher ratio, since all the created charge drifts in high weighting field region in the same time (see e.g. illustration of a induced pulse at Fig. 13). On the other hand, in a multi-site event energy is deposited in multiple places in the detector and during the drift a superposition of single-site pulses is observed (Fig. 8). However, the maximum amplitude is lower in this case (for two events with equal deposited energy the area under the current pulse must be the same in both cases).

The A/E analysis was performed using the following algorithm, described already in [18, 19]:

- Baseline subtraction of the charge pulse.
- Removal of the exponential tail from the charge pulse using pole-zero cancellation. The pole corresponding to

the falling tail was found by fitting an exponential function to the tail.

- The current pulse was obtained by applying the moving window deconvolution (MWD) to the charge pulse with a time constant of 40 ns.
- The current pulse was then smoothed by applying 3 times the moving window averaging (MWA) filter with a time constant of 50 ns.
- The value of A was determined by finding a maximum of the smoothed current pulse.

MWD and MWA time constants (as well as the number of MWA passes) were optimized to get the best multi-site events rejection efficiency.

The next step was the energy dependence correction of the A/E classifier. A following function was fitted to the A/E

distribution for a number of energy intervals:

$$f(A/E) = \frac{n}{\sigma_{A/E} \sqrt{2\pi}} e^{-\frac{(x-\mu_{A/E})^2}{2\sigma_{A/E}^2}} + m \frac{e^{f(x-l)} + d}{e^{(x-l)/l} + l}. \quad (6)$$

Values of $\mu_{A/E}$ as a function of energy were then used for a linear regression to determine the coefficients of the energy dependence. With the known energy dependence it was possible to correct the A/E value for each event such that the mean value of the distribution is equal to 1 for all energies.

To compare the efficiency of the A/E method the cut was set to the same acceptance of events in the DEP, namely 90%. The results for ^{228}Th are compared in Table 1. By analyzing survival probabilities in SEPs and FEPs it can be concluded that for this prototype detector the ANN-based PSA provides better multi-site events rejection efficiency. A similar behaviour was observed for the analysis described in [20]. However, it should be noted that for much more massive ($\approx 0.5\text{ kg} - 0.7\text{ kg}$) BEGe detectors used in GERDA the A/E method provides much better multi-site events rejection efficiencies [17] as obtained here.

A probable hypothesis why the PSA efficiency for the described prototype detector is relatively low are geometrical effects, which influence the pulse shapes. For larger detectors the drift times from the outer edges to the p^+ contact are much longer. This is a favorable effect from the pulse shape analysis point of view, since the current pulses corresponding to energy depositions at closer and further radii can be much easier distinguished – the current peak visible in Fig. 8 is induced only when charge carriers are drifting near the p^+ contact. Therefore, if the two point have much different drift times there will be an easily distinguishable signature in the pulse shape.

For the A/E analysis results the obtained efficiency in rejection of the 2614.5 keV peak is significantly worse than for the 1620.5 keV peak. Since both peaks contain mostly multi-site events one would expect, after removing the energy dependency of the A/E classifier, a similar efficiency in multi-site events rejection. While the exact reason of the discrepancy is not clear to the authors, it is consistent with the A/E analysis results reported in [37], where 24% and 31% of events from 1620.5 to 2614.5 keV FEPs, respectively, survived the cut. On the other hand, the ANN-based PSA gives more consistent result for the detectors described above (this work and [20]). However, this discrepancy should not be regarded as a property of the A/E classifier. For most of the detectors analyzed in [17] there is a good agreement on survival probability between 1620.5 and 2614.5 keV FEP (with the exception of two, where the difference is larger than 4%).

Since the ANN based PSA provided better MSEs rejection efficiency for the described prototype detector, it was used

as a main method for analysis of other acquired datasets. Moreover, the ANN approach does not require any energy corrections. Even if the band of SSEs and MSEs show some energy dependence they are still clearly separated in the whole energy range – see, e.g. Fig. 6. The cut is robust, namely variation of the discrimination parameter (as long as it is placed in the valley between the bands) provides similar values of surviving probabilities.

4.2 Application of PSA to the ^{56}Co spectrum

The analysis method based on ANN provides an attractive option for the recognition of patterns, waveforms and other observables. The network can recognize subtle details in the analyzed data, which would be otherwise hard to describe analytically. However, in some cases unrealistically high recognition efficiencies may be generated – this phenomenon is called “over-training”. It may appear when, e.g., the training samples are too poor to work out a general pattern recognition in the ANN. Instead, the ANN discriminates between the events used for training, but does not recognize the difference in the ones that were not used in the training dataset.

In order to have an independent cross check of the investigated PSA method, we applied the cut defined for ^{228}Th to the data acquired by irradiating the detector with a ^{56}Co source. From the PSA point of view ^{56}Co is very well suited for this kind of tests, because it emits a series of high energy γ -rays: 2598.5 keV (intensity 17.3%), 3201.9 keV (intensity 3.2%) and 3253.4 keV (intensity 7.9%) — which allow for an independent evaluation of the survival efficiencies in multiple energy regions. The above mentioned FEPs are an excellent source of MSEs for testing, but they also give rise to DEPs, with most prominent ones at 1576.5 keV and 2231.5 keV. This provides an opportunity to test the acceptances of single-site events important for the experiments looking for the $0\nu\beta\beta$ decay in ^{76}Ge . Especially the 2231.5 keV DEP is of special interest since it is close to $Q_{\beta\beta}$, where the signal peak is expected to be observed in the energy spectrum ($Q_{\beta\beta} = 2039\text{ keV}$).

The ^{56}Co source was produced in the $^{56}\text{Fe}(p,n)^{56}\text{Co}$ reaction. Three Fe foils (10 mm in diameter and 0.1 mm thick, acquired from Goodfellow) were irradiated using the proton beam on AIC-144 cyclotron in IFJ PAN. Since ^{nat}Fe has high isotopic abundance of ^{56}Fe (91.7%), it was not necessary to use an enriched foil for the source production. AIC-144 cyclotron has the nominal output energy of 60 MeV per nucleon, but $^{56}\text{Fe}(p,n)^{56}\text{Co}$ reaction cross section has a maximum around 12 MeV/nucleon [38] therefore, it was necessary to use a proton energy degrader. After 8 hours of irradiation the Fe foils were measured together with an HPGe spectrometer for the ^{56}Co activity determination, which was $\approx 80\text{ kBq}$. Only one foil was used then to acquire the ^{56}Co spectrum with the prototype detector.

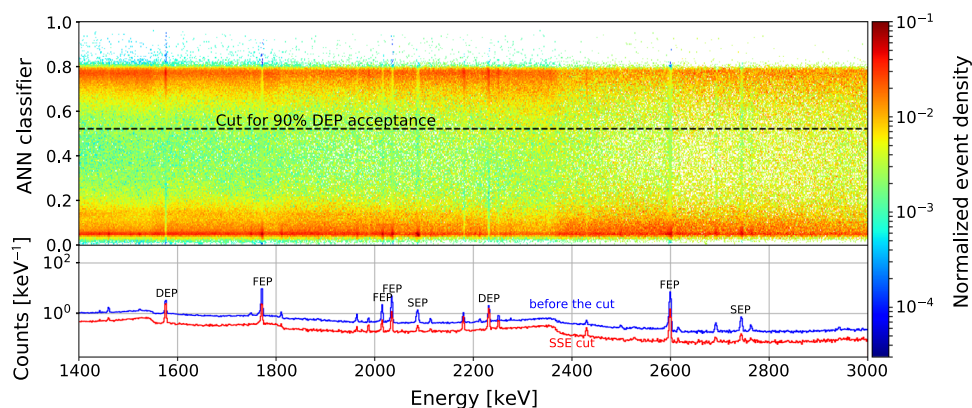
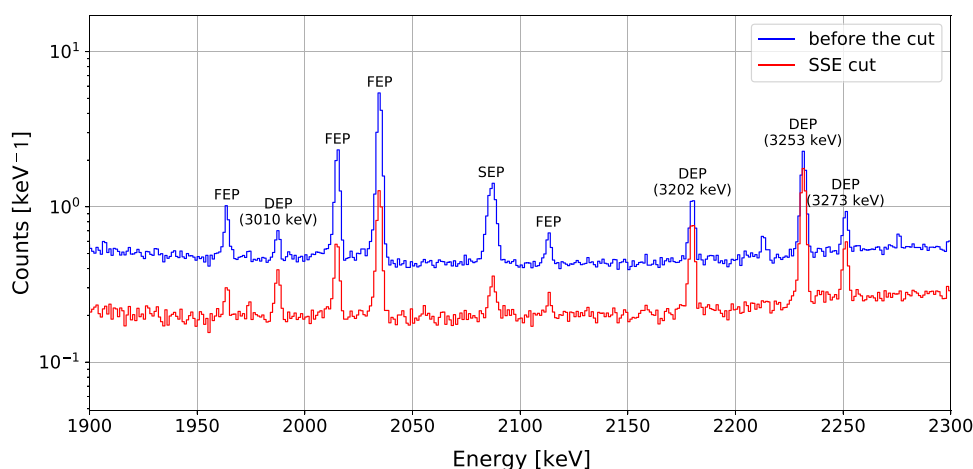


Fig. 9 2D histogram showing the classified ^{56}Co events distribution. Vertical axis corresponds to the classifier value (ANN) and the horizontal one to the reconstructed energy. The bottom panel shows the corresponding energy spectra (before/after the cut). Two bands with

increased single- and multi-events densities are clearly visible – a similar structure like for the ^{228}Th data. The cut at ANN = 0.52 from training performed on ^{228}Th was applied

Fig. 10 Close-up of the ^{56}Co spectrum before and after the cut rejecting MSEs (the same spectrum as in the bottom panel of Fig. 9), showing the effect of the PSA method on peaks consisting of events of different types. Suppression of MSEs in SEPs and FEPs is clearly visible, while SSEs in the DEPs are mostly accepted



The same analysis chain as in the case of ^{228}Th data was applied to the ^{56}Co spectrum. This includes application of the quality cuts (rejection of unphysical events), energy reconstruction, energy calibration and classification. Classification of events was based on the training performed on the ^{228}Th data (the cut set to preserve 90% of events from DEP). A 2D histogram containing the classified events from ^{56}Co dataset is shown in Fig. 9. A similar two-band structure can be observed as in the case of ^{228}Th , with a clear separation of single- and multi-site events. The obtained acceptances are collected in Table 2 – the peaks were sorted according to their energies and types for an easier comparison.

Comparing to the ^{228}Th data, suppression of multi-site events from FEPs was at a very similar level (between 20 and 24% for both data sets – see Tables 1 and 2). A slight energy dependence is however noticed – at higher energies the FEP events are rejected more efficiently. The slope shown in Fig. 11 is $-9.1\text{ \%}/\text{MeV}$. Events from SEPs were affected stronger by the cut in the ^{56}Co data (reduction down to 16%

for ^{228}Th and down to 12% for ^{56}Co), what is most probably a result of different event topologies (multiple Compton scatterings and a photoelectric absorption for FEP vs. pair production, (optional) Compton scatterings and a photoelectric absorption for SEP). Events from the two ^{56}Co DEPs show only very little energy dependence in terms of PSA survivability (90% acceptance at 1576.5 keV vs. 85.6% at 2231.5 keV) and their survival fraction is very close to the definition set for ^{228}Th DEP. The cut effect is visualized on the energy spectra before and after the cut in Fig. 10. Thus, one can conclude that the PSA performed on the ^{56}Co data with the ANN trained on the ^{228}Th data delivers results consistent with these obtained for the ^{228}Th spectrum.

5 Pulse shape simulation

A possibility to simulate properly the pulses (their shapes) generated by a detector with a certain geometry would allow to optimize the design of HPGe detectors (size/dimensions of

Table 2 Acceptances of events in various peaks present in the ^{56}Co spectrum. Training of the neural network was performed on ^{228}Th data assuming 90% survival efficiency of the 1592.5 keV DEP

Energy (keV)	Peak type [intensity (%)]	Acceptance (%)	Energy (keV)	Peak type [intensity (%)]	Acceptance (%)
1175.1	FEP (2.3)	23.9 ± 1.2	2598.5	FEP (17.0)	20.3 ± 0.3
1238.3	FEP (66.5)	23.2 ± 0.1			
1360.2	FEP (4.3)	19.9 ± 0.7	1576.5	DEP	90.1 ± 1.2
1771.4	FEP (15.4)	22.2 ± 0.3	2231.5	DEP	85.6 ± 1.4
2015.2	FEP (3.0)	21.1 ± 1.1			
2034.8	FEP (7.8)	22.1 ± 0.5	2087.5	SEP	11.7 ± 1.6

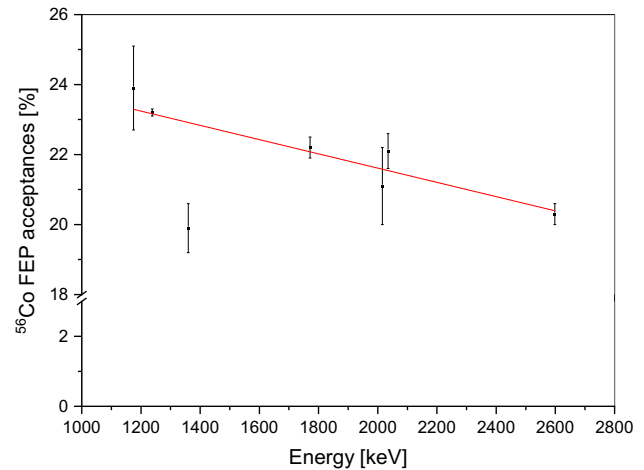
the crystal, geometry of the electrodes, impurity level and its gradient) with respect to the PSA performance. First of all, the optimized geometry would allow to achieve the lowest possible depletion voltage and therefore, to operate the detector at the bias, which would minimize the charge recombination effects and still avoid high leakage current (it degrades the energy resolution due to excessive noise). From the data plotted in Fig. 2 it is clear that for the prototype detector the leakage current is starting to rise at the bias voltage significantly higher (1100 V) than the depletion voltage (800 V). The leakage current is a product of many factors, like contact fabrication technique, quality of the passivated surface or the detector's temperature. Nonetheless, for the same detector manufacturing technology and the same operating conditions, it is still possible to optimize the depletion voltage with respect to e.g. the contact size, width of the groove or the amount passivated area. From the point of view of the energy resolution, which is important for the applications like the $0\nu\beta\beta$ decay, Dark Matter searches and γ -ray spectrometry, minimizing the detector capacitance offers lower noise levels.

Another important factor is the PSA efficiency to recognize MSE and SSEs, especially with respect to the background reduction in the $0\nu\beta\beta$ decay experiments based on HPGe detectors. Since it obviously depends on the shapes of the event pulses, which are in turn a function of the detector geometry, impurity concentration and bias voltage, some optimization is also possible in this regard.

The simulations performed for the prototype detector were based on the ADL package [39], similarly as earlier attempts described in the literature [39–41]. Our advantage was that we knew all the parameters of the detector/crystal, including also the response of the preamplifier and the noise of the spectroscopic chain. Therefore, we were in a position to precisely fine tune the model by comparing its output with the corresponding experimental data.

The steps of the simulation procedure are listed below with the details explained in the following sections:

1. Implementation of the exact geometry of the detector and cryostat setup in GEANT4.

**Fig. 11** Acceptance of the FEP events as a function of energy for the ^{56}Co spectrum

2. Simulation of energy depositions in the detector by the γ -rays with GEANT4.
3. Calculation of electric and weighting fields in the detector using ADL4.
4. Tracking of charges from each interaction point, the drift of holes and electrons was calculated using the electric field obtained in the previous step.
5. Convolution of the calculated pulse shape with the preamplifier response, addition of the baseline and noise traces.

5.1 Energy deposition

In the first step of the simulation chain a detailed geometry of the detector and the cryostat was implemented in GEANT4. It is shown in Fig. 12. Two datasets were simulated for two different γ -ray sources: ^{228}Th and ^{56}Co . In the simulation they were placed on the detector's endcap (reproducing the conditions in which the measurements were performed). For every event the positions of the interaction points and the deposited energy were recorded for later use to calculate the pulse shapes.

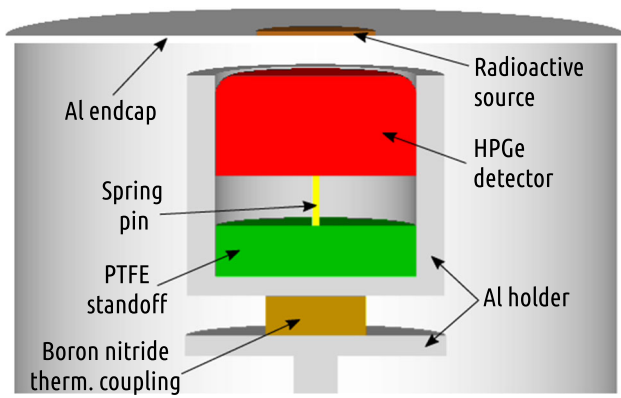


Fig. 12 Detector-cryostat geometry as implemented in GEANT4. The detector holder, as well as the PTFE standoffs and the readout pin, are all taken into account in the simulation. Radioactive sources are placed on top of the aluminum endcap

5.2 Calculation of electric field in the detector

In the second step of the simulations the electric and weighting fields in the detector were calculated using the ADL package. To accomplish that, apart from the geometry, the crystal parameters like the impurity concentration and its distribution had to be known. This information was available from Umicore, for example the acceptor impurities concentrations were given to be $N_A = 0.58 \times 10^{10}$ and $0.48 \times 10^{10} \text{ cm}^{-3}$ at the top and bottom planes, respectively (we assumed a linear gradient). The electric field governs the drift of the carriers (electrons and holes) inside the detector, because their velocities depend directly on the field amplitude and direction. The field is calculated numerically by solving the Poisson equation:

$$\nabla^2 \phi(\mathbf{r}) = -\frac{\rho}{\epsilon \epsilon_0}, \quad \rho = -q N_A \quad (7)$$

where, ρ is the charge density, N_A – the acceptor impurities concentration, $\phi(r)$ – the electric potential and $\epsilon \epsilon_0$ is the product of the germanium dielectric constant and the vacuum permittivity. The boundary conditions assume a potential of 0 V on the p^+ contact and the operational bias voltage on the outer electrode (n^+ , 1100 V).

The electric field formed in the prototype detector is shown in Fig. 13 (left panel). It is the strongest in the vicinity of the p^+ electrode. The same is true for the weighting field (middle panel of Fig. 13), which for small anode detectors (like BEGe and point-contact geometries) is responsible for the peaked structure in the current signal allowing for effective PSA. An example of a charge trajectory is shown as a white line – the electron-hole pair was created near the rounder edge of the detector (upper right part of the graph, red star). The created electron is immediately collected on the outer n^+ electrode, while the created hole travels through the detector to be collected on p^+ contact (coordinate $\approx (x, y) = (0, 0)$). The movement of the hole induces the charge pulse represented by the blue waveform shown in the right panel of Fig. 13.

5.3 Calculations of the pulse shapes

The movement of the charges depends on the electric field in the detector. However, the induced signal on the readout electrode is calculated using a mathematical construct called the weighting field/potential. According to the Ramo–Shockley theorem, the induced current is given as:

$$i_{e,h}(t) = \pm q \mathbf{v}_{e,h}(t) \cdot \mathbf{E}_w(\mathbf{r}), \quad \mathbf{r} = \mathbf{r}(t) \quad (8)$$

where (bold font indicates vector variables):

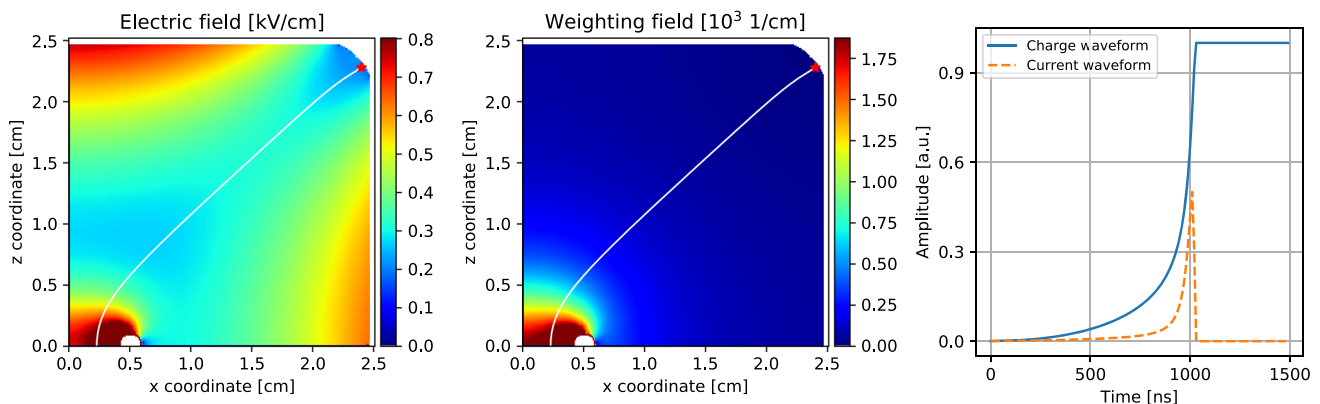


Fig. 13 Simulated electric field (left panel), weighting field (central panel) and an example of a pulse induced in the detector. The induced charge (blue continuous line in the right panel) corresponds to the trajectory marked with the white lines on the left and the central pan-

els, originating from the γ -ray interaction point (red star). The current waveform (orange dashed line, right panel) is a derivative of the charge waveform

- $i_{e,h}(t)$ is the current induced by a movement of the charge carriers,
- $\mathbf{v}_{e,h}(t)$ is the charge carrier velocity in a given time moment t ,
- $\mathbf{E}_w(\mathbf{r})$ is the weighting field at the point \mathbf{r} ,
- $\mathbf{r}(t)$ is the position of the drifting charge carrier in a given time moment t .

The weighting field is calculated using the Laplace equation: $\nabla^2 \phi_w(r) = 0$ assuming the potential to be 1 at the readout electrode and all other electrodes grounded. The concept of the weighting potential may seem confusing at first, but it is important to see it as a mathematical tool to calculate the induced current. For a multiple electrode detector (e.g. a segmented HPGe detector) the weighting field needs to be calculated for each readout electrode with separate boundary conditions.

Another important remark is that while the current is calculated as a function of time, the weighting field is defined spatially. Therefore, it is necessary to calculate the trajectory $\mathbf{r}(t)$ first and then the weighting field as a function of time for this trajectory ($\mathbf{E}_w(t) = \mathbf{E}_w(\mathbf{r}(t))$).

At a first glance it may also seem that the induced current does not depend on the electric field. However, as it was stated before, both, the trajectory and the drift velocity depend on the electric field so, as in the case of weighting field, the velocity has to be calculated along the given trajectory and then used in the Ramo-Shockley equation. From the equation's point of view the mechanism which causes the charge to move is not important, what matters is the scalar product between the velocity and the weighting field.

5.4 Convolution with the preamplifier response and noise

Pulses obtained from ADL do not include effects related to the readout chain. The two main ones, which need to be taken into account, are the limited bandwidth of the preamplifier and the presence of electronic noise. To include them in our simulations appropriate measurements were performed. The first one aimed to determine the response of the preamplifier and was done by feeding a fast (rise time < 5 ns) rectangular signal pulses to the test input of the preamplifier. An example of the response, recorded with a fast oscilloscope (sampling rate of 1 GHz and 8 bit resolution), is plotted in the upper panel of Fig. 14. In the lower panel of Fig. 14 an averaged pulse is shown.

Since the response signal contained noise, we took some measures to reduce it. Firstly, the signal was down sampled (to the sampling rate of the FADC, 100 MHz) by averaging each ten neighboring amplitudes. This operation reduced some noise and improved the amplitude resolution. Then, after horizontal alignment and baseline subtraction, 1000 pulses were summed together and normalized amplitude-

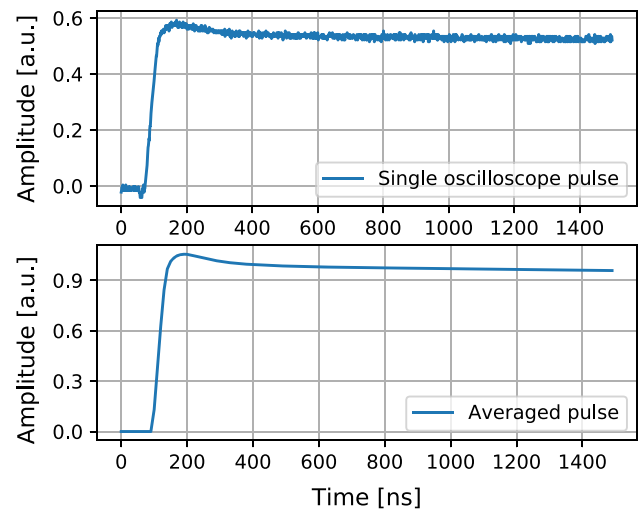


Fig. 14 Impulse response of the preamplifier. The top panel shows a single waveform captured by the oscilloscope. It was induced with a fast (rise time < 5 ns) square pulse fed into the test input of the preamplifier. The bottom panel shows the response with the noise removed: for each single waveform ten consecutive points were averaged together and then 1000 of such waveforms were added and normalized (after the horizontal alignment)

wise. The resulting pulse is plotted in the bottom panel of Fig. 14. The averaging procedure removed the noise and preserved the rising edge of the signal. We did not apply any other filtering procedures, like, e.g., a moving average filter, which would decrease the bandwidth of the signal and possibly create simulated pulses which are slower than their real life counterparts. Figure 15 illustrates the consecutive steps in applying the electronic response to the simulated pulses. It should be noted that the simulated signal is a charge pulse rather than a current one. Since the measured preamplifier response model assumes a current signal at the input, the simulation output has to be differentiated before the convolution.

To include effects of the finite energy resolution, the amplitude of the pulse and its energy, obtained from GEANT4, were scaled according to the energy value with a random number from a Gaussian distribution (with a sigma corresponding to the given energy, obtained from the FWHM vs. energy curve in the bottom panel of Fig. 5, $\sigma \approx \text{FWHM}/2.35$). This way the energy resolution degradations coming from the charge carriers generation statistics and possible charge trapping were taken into account. A separate measurement was performed to record noise waveforms at the preamplifier's output. It was added in last step to the simulated pulses convoluted with the electronic response, as shown in Fig. 15.

It should be noted that since in the analysis the pulses are normalized according to the energy value, the Gaussian smearing is effectively canceled out. It still affects the selection of events for both training and classification by the ANN,

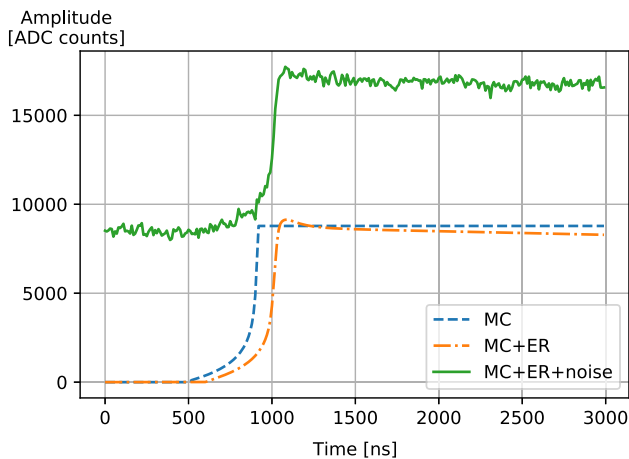


Fig. 15 Implementation of the preamplifier response (ER) and the addition of electronic noise to the simulated pulses (MC). The blue dashed line represents the calculated pulse and the orange dashed the convolution of pulse with the preamplifier response. After adding the noise (recorded separately) one gets the final shape of the pulse

since they are chosen using a cut on the energy spectrum. However, the addition of the noise trace introduces some uncertainty in the amplitudes of the samples used on the neural network input, which in turn influence the PSA performance, which is a desired effect to obtain simulation results corresponding to those obtained from the measurement.

Another way to introduce the noise in the simulation would be to reconstruct the energy based only on the filtered waveform, as it is done for the measured data and effectively avoid the Gaussian smearing. Unfortunately, this is not the right approach, since it does not take into account the previously mentioned phenomena of charge carriers statistics and trapping effects, which are random and also introduce uncertainty in the amplitude and pulse shape measurement.

5.5 Results of the pulse shape simulation

Simulated energy spectra for ^{228}Th and ^{56}Co sources are compared with the real data in Fig. 16. A good agreement is observed in the 1000 keV–3000 keV energy range, which is of main interest from the PSA point of view. Some discrepancies are visible in the lower energies, which could result from the uncertainties regarding the geometry and material composition of the detector endcap and the holder models in GEANT4. For ^{228}Th at energies above 2.6 MeV the simulation predicts more counts due to summing effects, which are difficult to precisely model in the Monte Carlo software.

After obtaining a set of simulated pulses for the ^{228}Th source, ANN was trained again, this time on the simulated data. Afterwards, the analysis was applied to classify the simulated ^{228}Th and ^{56}Co data.

The corresponding 2D distribution of the ^{228}Th events (classifier value vs. energy) looks very similar to the one

obtained while training on the measured data (Figs. 17 and 6, respectively). The two bands are clearly visible, however they are more narrow for the simulated data than for the measured dataset. In Table 3 we compare the PSA efficiencies of the method trained on the measured (first column) and on the simulated datasets. The simulations were performed for various temperatures (Table 3) which affect the drift velocity of electrons and holes inside the crystal. The temperature of the detector holder was measured using a PT100 sensor and it was equal to 82 K. However, the best agreement between the simulated and the measured data is obtained for 50 K for which the drift velocity is higher. Since the exact drift velocity profile was not measured separately for the used crystal, we treated the temperature as a free parameter in the simulation. Lowering this “effective” temperature even further did not provide any better agreement between the analyses for simulated and measured data. Therefore, we have chosen 50 K as the temperature for all presented comparisons. Figure 18 shows the effect of the PSA cut on the peaks in ^{228}Th spectrum for that optimal temperature (50 K).

The same ANN was also used to classify the events from ^{56}Co dataset – the acceptances of the events after the application of the PSA cut are gathered in Table 4. The acceptance of the FEP events from ^{56}Co is at the same level as for their counterparts from the ^{228}Th dataset (within a few percentage points). Furthermore, we observed almost no difference in acceptance of DEPs, while for the measured data there was a $\approx 4.5\%$ difference. This means that there is either an amplitude-dependent effect in the preamplifier or an energy dependent effect on the pulse shape from the detector. Table 4 contains also the differences in acceptances of events ($\Delta_{\text{Meas.}-\text{MC}}$) between the simulated and the measured datasets (Table 2). The results agree well for all analyzed peaks – the differences are below 4% points.

Figure 19 shows an energy dependence of acceptances for the simulated ^{56}Co FEPs. As in the case of measured spectrum there is a noticeable effect: events of higher energies are rejected more efficiently but the difference is only about 4% between 1175.1 and 2598.5 keV (slope of 2.8%/MeV).

5.6 Cross-check of the simulated and measured data

An important feature of the simulation software is how well the simulated pulses are reproducing the measured ones. MC simulations could help to understand better the separation effect between SSEs/MSEs and estimate the systematic uncertainties of the events classification with PSA methods based on neural-networks. This is not possible using only the measured data, because e.g. it is known that the DEP events from the ^{228}Th spectra used to train the network are not homogeneously distributed in the detector volume. Most of these events are localized close to the edges of the detector, where it is the easiest for the two 511 keV annihilation

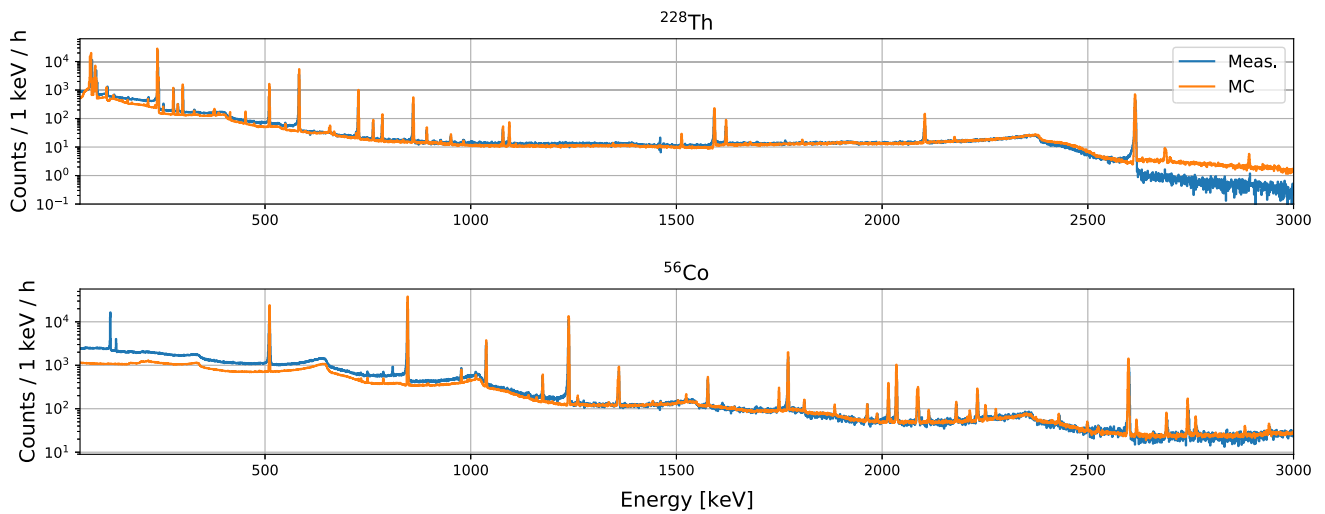


Fig. 16 Comparison of the measured and simulated energy spectra acquired with ^{228}Th (top panel) and ^{56}Co (bottom panel) sources. A good agreement is achieved in the 700 keV–3000 keV range, which is the region of interest of the investigated PSA method. The measured

^{56}Co spectrum contains also contributions from ^{57}Co and ^{58}Co – isotopes, which are also created in the proton activation (not included in the simulation, since they contribute only in the lower energy range)

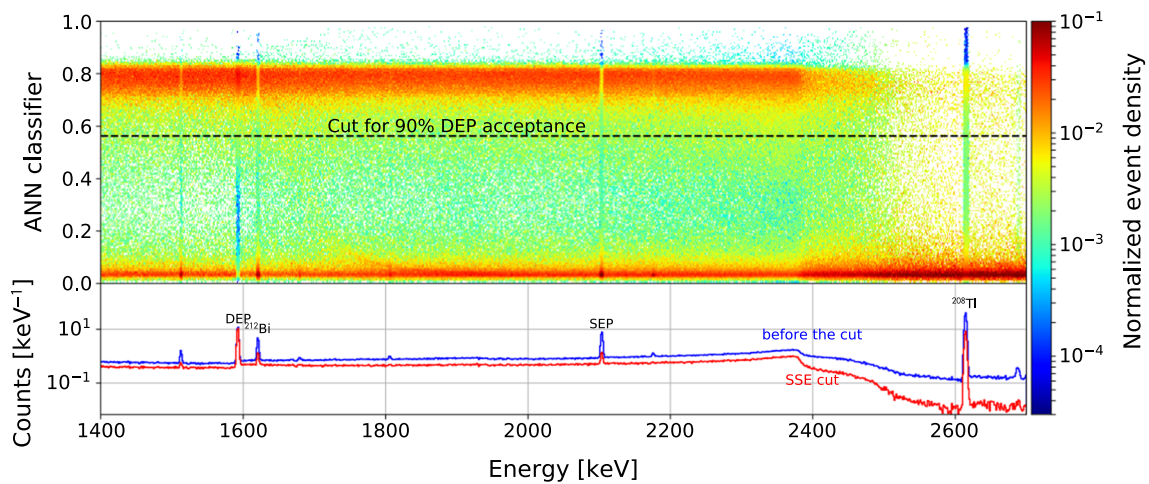


Fig. 17 2D histogram showing distribution of the classified ^{228}Th events (simulated for the temperature equal to 50 K). The bottom panel shows the corresponding energy spectrum. For comparison with the measured data see Fig. 6

Table 3 Comparison of the acceptances for events from the ^{228}Th dataset (third column) and for the simulated pulses (various temperatures). The best agreement is obtained for 50 K. The temperature in the simulation is treated as a parameter influencing the charge drift velocities

Energy (keV)	Peak type	Meas. data	30 K	40 K	50 K	60 K	70 K	80 K	90 K
1592.5	DEP	89.98	90.0 ± 0.3	90.1 ± 0.3	90.0 ± 0.3	90.0 ± 0.3	90.0 ± 0.3	90.1 ± 0.3	90.0 ± 0.3
1620.5	^{212}Bi	23.12	21.4 ± 0.7	21.1 ± 0.7	21.0 ± 0.7	20.5 ± 0.7	19.6 ± 0.7	19.1 ± 0.7	18.2 ± 0.7
2103.5	SEP	15.89	13.2 ± 0.5	13.1 ± 0.5	12.7 ± 0.5	12.1 ± 0.5	11.5 ± 0.5	10.7 ± 0.5	10.4 ± 0.5
2614.5	^{208}Tl	20.3	20.9 ± 0.1	21.2 ± 0.1	20.6 ± 0.1	19.7 ± 0.1	18.9 ± 0.1	18.1 ± 0.1	17.1 ± 0.1
Cut value for 90% DEP acc.		0.52	0.56	0.56	0.56	0.57	0.58	0.59	0.60

Fig. 18 Close-up of the ^{228}Th (pulses simulated at 50 K) spectrum before and after the cut rejecting MSEs (the same spectrum as in the bottom panel of Fig. 17), showing the effect of the PSA method on peaks consisting of events of different types. Suppression of MSEs in SEPs and FEPs is clearly visible, while SSEs in the DEPs are mostly accepted

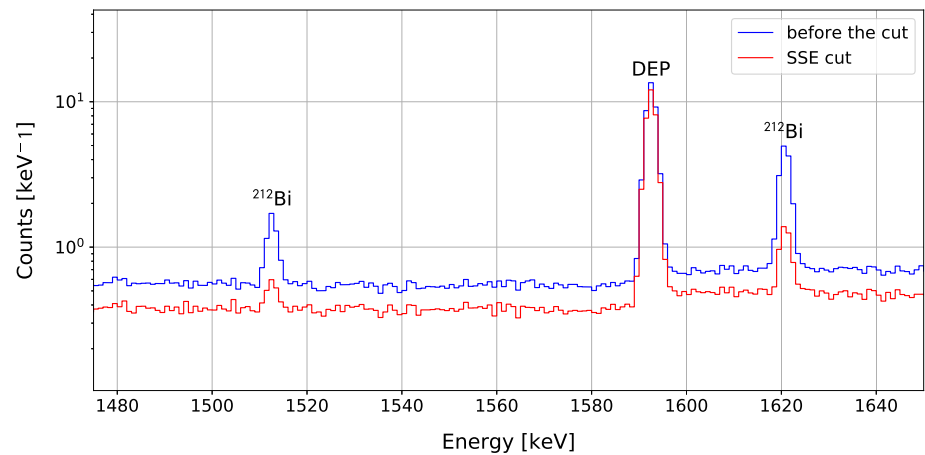


Table 4 Acceptances for events in various energy regions for simulated ^{56}Co dataset after the PSA cut. It was defined using the simulated ^{228}Th data (requesting 90% survival fraction of the 1592.5 keV DEP). The last

column contains differences in acceptance between the simulated and measured data (Table 2)

Energy (keV)	Peak type [intensity (%)]	Acceptance (%)	$\Delta_{\text{Meas.-MC}} (%)$	Energy (keV)	Peak type [intensity (%)]	Acceptance (%)	$\Delta_{\text{Meas.-MC}} (%)$
1175.1	FEP (2.3)	22.5 ± 0.8	-1.4	2598.5	FEP (17.0)	21.1 ± 0.2	0.8
1238.3	FEP (66.5)	22.2 ± 0.1	-1.0	1576.5	DEP	89.1 ± 0.8	-1.1
1360.2	FEP (4.3)	16.2 ± 0.4	-3.8	2231.5	DEP	89.4 ± 0.9	3.8
1771.4	FEP (15.4)	21.6 ± 0.2	-0.5	2087.5	SEP	7.8 ± 0.6	-4.0
2015.2	FEP (3.0)	21.4 ± 0.6	0.3				
2034.8	FEP (7.8)	21.7 ± 0.3	-0.4				

γ -rays to escape. The bigger the crystal the more significant this effect is. Realistically simulated SSEs would be therefore more suitable for training. Another option, very attractive from the perspective of the $0\nu\beta\beta$ decay searches, would be to use for ANN training simulated signals corresponding to the $2\nu\beta\beta$ decays in the detector's volume. This would be possible by using DECAY0/DECAY4 event generators [42], which take into account the kinematics of the ^{76}Ge $0\nu\beta\beta$ and $2\nu\beta\beta$ decays by using the theoretical models. Since there are some differences in the ionization resulting from single-site events originating from a pair production (DEP events) and those from the $0\nu\beta\beta$ decays, events generated by DECAY0 could provide more precise event topologies and signal shapes.

In our approach we applied the ANN cuts defined on the MC data to classify the measured pulses (MC/Meas.) and vice versa (Meas./MC). The distributions of events as a function of the classifier value/energy for ^{228}Th are shown in Fig. 20 and in Fig. 21 for the (MC/Meas.) and (Meas./MC) scenarios, respectively. In both cases the characteristic two band structure is visible, indicating a good separation between reproduced single- and multi-site events. Corresponding acceptances, also for (Meas./Meas.) and (MC/MC) options (training/classification on data and training/classification on simulated pulses, respectively) of events from various energy

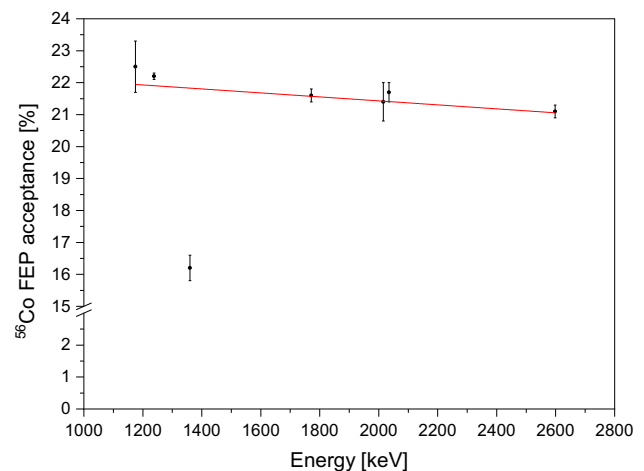


Fig. 19 Acceptance of the FEP events as a function of energy for the simulated ^{56}Co spectrum

regions of the ^{228}Th spectra are collected in Table 5. The effect of the PSA cut on various peaks from ^{228}Th spectra is visualized in Figs. 22 and 23, for ANN trained on MC and measured pulses, respectively.

From the data (Table 5) one can conclude that all considered scenarios provide similar results with respect to the acceptances of the multi-site events (from FEPs and SEP).

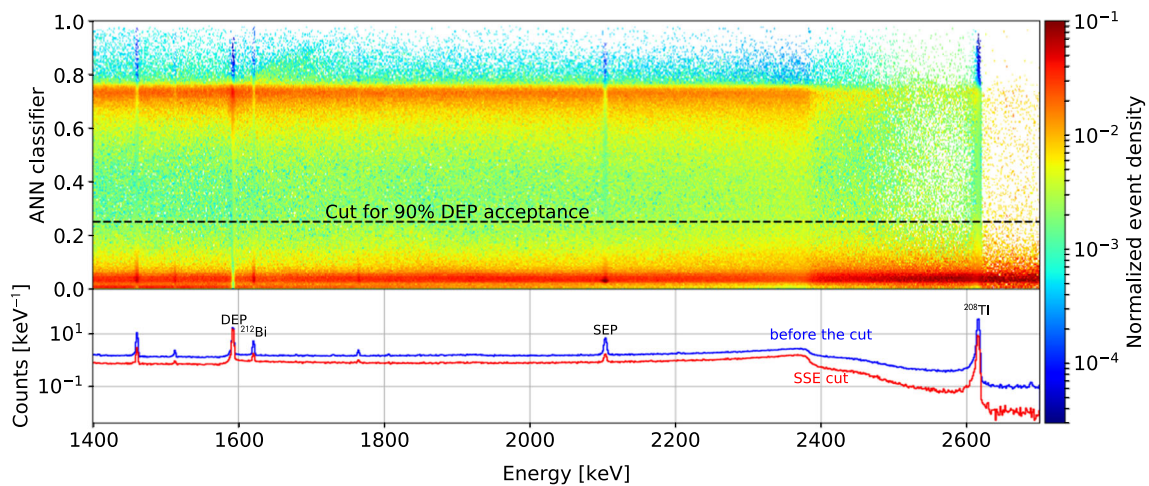


Fig. 20 2D histogram showing the classified ^{228}Th events (measured data) with ANN trained on the MC data. The bottom panel shows the corresponding energy spectra (before/after cut). SSEs and MSEs are

well separated. The numerical values of survival fractions for various peaks are presented in Table 5 (column denoted with MC/Meas.)

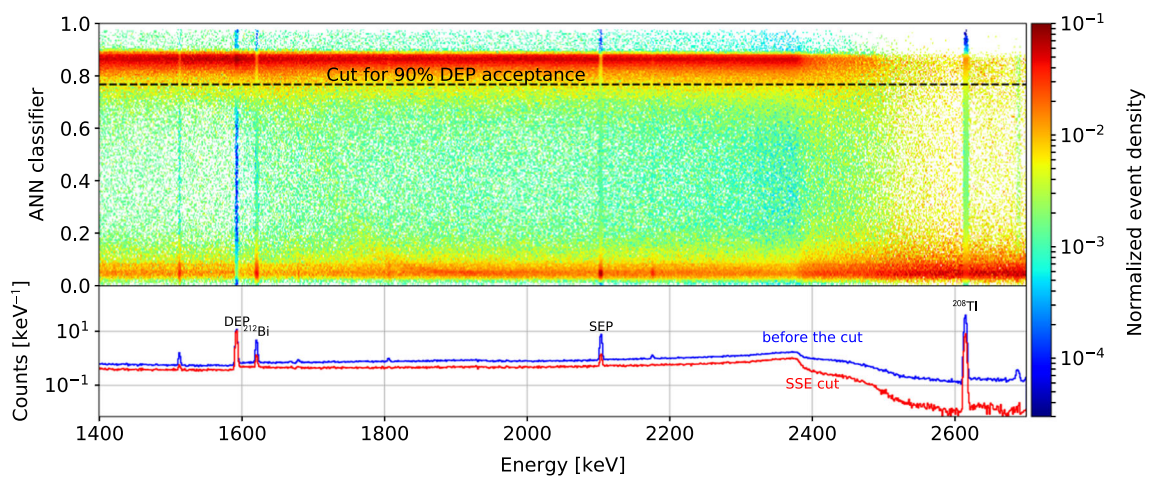


Fig. 21 2D histogram showing the classified ^{228}Th events (MC data) with ANN trained on the measured data. The acceptances for various peaks are included in Table 5 (column denoted with Meas./MC)

Fig. 22 Close-up of the ^{228}Th (ANN trained on MC pulses, real data classified) spectrum before and after the cut rejecting MSEs (the same spectrum as in the bottom panel of Fig. 20), showing the effect of the PSA method on peaks consisting of events of different types. Suppression of MSEs in SEPs and FEPs is clearly visible, while SSEs in the DEPs are mostly accepted

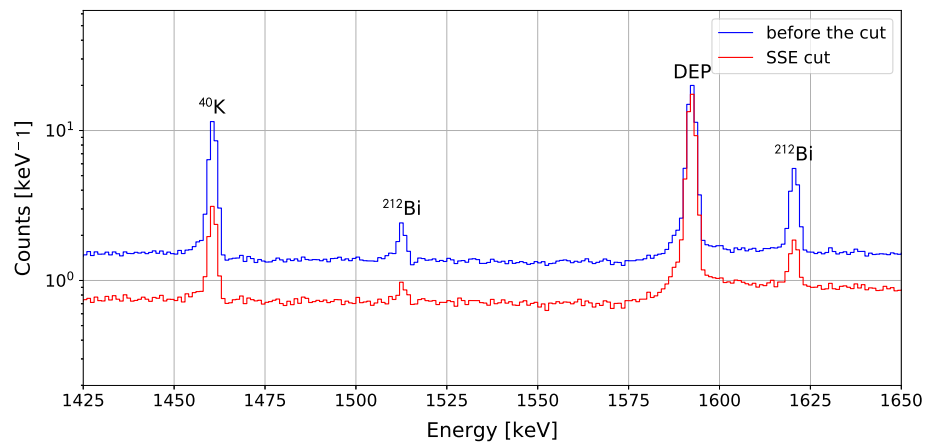


Fig. 23 Close-up of the ^{228}Th (ANN trained on real pulses, MC data classified) spectrum before and after the cut rejecting MSEs (the same spectrum as in the bottom panel of Fig. 21), showing the effect of the PSA method on peaks consisting of events of different types. Suppression of MSEs in SEPs and FEPs is clearly visible, while SSEs in the DEPs are mostly accepted. ^{40}K peak is not present in this spectrum, since only decay chain of ^{228}Th was simulated

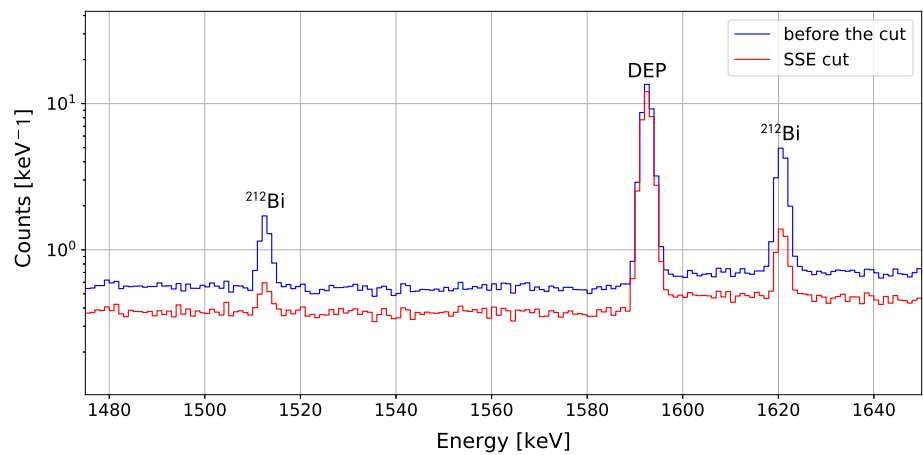


Table 5 Event survival fractions for different training/classification options for the simulated and measured ^{228}Th data. (Meas./Meas.), (MC/MC), (Meas./MC) and (MC/Meas.) denote the scenarios when: ANN was trained and applied to the measured data, ANN was trained and applied to the simulated data, ANN was trained on the measured data and applied to the simulated one and vice versa, respectively. The first two options were discussed earlier and were included for comparison purposes

Peak	Acceptance (%)			
	Meas./Meas.	MC/MC	Meas./MC	MC/Meas.
DEP	90.0 ± 0.3	90.0 ± 0.3	90.1 ± 0.3	90.0 ± 0.3
^{212}Bi	23.1 ± 1.0	21.0 ± 0.7	20.6 ± 0.7	24.6 ± 1.1
SEP	15.9 ± 0.6	12.7 ± 0.5	13.0 ± 0.5	16.8 ± 0.6
^{208}Tl	20.3 ± 0.1	20.6 ± 0.1	20.0 ± 0.1	23.1 ± 0.1

The relative differences are at most at the level of 13%, comparable with the systematic uncertainties of the presented survival fractions. This confirms that the precise modeling of the detector (using relevant input, like the impurity concentration and geometry of the contacts) and electronics response provides reliable Monte Carlo simulations of the pulse shapes.

6 Capacitance simulation

Using the ADL software one can simulate the electric field only for a completely depleted diode – it is not possible to calculate the C–V curve for the bias voltages below the depletion voltage. To obtain this data and to compare it with the measurements, we used the *fieldgen* program, which is a part of the *siggen* software [43].

A comparison between the simulated and measured C–V curves is shown in Fig. 24. A very good agreement is observed and the depletion voltage of ≈ 750 V can be derived from both curves. The terminal (at full depletion) capacitance is equal to 2.7 pF and 2.9 pF for simulated and measured

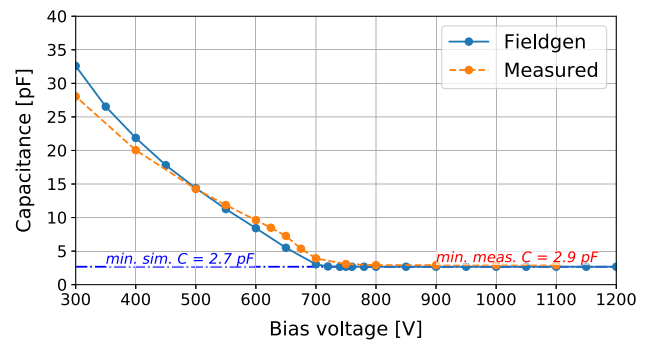


Fig. 24 Comparison of the simulated and measured C–V curves for the described prototype. The measured curve is the same as the one in Fig. 3. A good agreement between them can be observed for bias voltages over 500 V, while for the voltages below this value the simulated capacitance is lower than the measured one

data, respectively. An interesting feature is a rise in capacitance around ≈ 650 V – for this bias voltage also a sudden improvement of the FWHM was observed (Fig. 3). We suspect that this may be an effect called a “bubble depletion” or “pinch-off” [44–46], which often appears in the detectors with small anode geometry, like BEGe or point-contact types. It may be caused by a weaker electric field inside the detector appearing for certain bias voltage values.

7 Implications to future neutrinoless double beta experiments

In this paper we have described technology of a HPGe detector production, performed characterization (from the point of view of pulse shape analysis performance) and detailed Monte Carlo simulations. Acquired knowledge will help to improve sensitivities of running and future neutrinoless double beta decay experiments based on germanium in various ways:

- It may be possible to produce or repair/refurbish enriched HPGe detectors on-site, in an underground laboratory. This will minimize the cosmogenic activation of the detector material and also deposition of the long-lived radon daughters during handling. Consequently, the background and the sensitivity of an experiment will improve.
- By applying different sources (^{228}Th and ^{56}Co) we have shown that our neural network based PSA analysis is very robust and effective. Training and verification may be applied interchangeably to various data sets with very consistent results. ANN-based PSA applied to the data acquired with the prototype detector is more efficient in separation of SSEs from MSEs compared to the widely used A/E method. Another ANN's advantage is its simplicity, there is no need for any corrections to the data to set the cut value. The latter requires various corrections and re-normalizations to define the cut. We will also study the ANN performance with respect to rejection of alpha-induced events, but from the experience with other data sets we suspect that it will be very effective [19]. Simplicity of the method makes it easy to automate, what will be important for ton-scale experiments with many detectors of various geometries.
- Knowledge about all the crystal/detector and preamplifier parameters made it possible to verify different calculations of the capacity or depletion voltage of the prototype detector and to determine the drift speed of the charges (expressed by the effective temperature). Finally, the simulated pulses match very well the measured ones. This opens possibilities to study the systematic effects in the pulse shape analysis (simulated pulses may be used for neural network training) and to study various detector geometries with respect to PSA performance (detector size/shape optimization). This will be important to minimize the number of channels (detectors) for the future experiments.

8 Conclusions and outlook

In this paper we described the manufacturing and characterization process of a HPGe detector with a small readout contact. The worked out procedures may be applied to bigger detectors with different geometries, enriched in ^{76}Ge , to be used in the experiments devoted to search for the $0\nu\beta\beta$ decay. The characterization included measurements and simulations of the I–V/C–V curves and investigations of the PSA performance on the real and simulated pulses. The obtained energy resolution and the PSA efficiencies were comparable with those for the best detectors from commercial vendors. A further improvement of the energy resolution could be achieved by applying the low capacitance front-end elec-

tronics, in contrast to the 2N4393 J-FET, intended for use with semi-coaxial detectors.

An approach to the pulse shape analysis based on the neural network has been presented. ^{228}Th calibration spectrum was used to train the method. A defined cut was then applied to the ^{56}Co data. From the PSA point of view ^{56}Co is very well suited for this kind of tests, because it emits a series of high energy γ -rays, which allow for an independent evaluation of the survival efficiencies in multiple energy regions. We have shown that the survival fractions of ^{56}Co DEPs were very close to 90% set for ^{228}Th DEP and acceptances of ^{56}Co FEPs showed a small energy dependence. A reverse process, namely training on ^{56}Co data and application to ^{228}Th , provided similar results.

We have also carried out a full simulation of the $^{228}\text{Th}/^{56}\text{Co}$ pulses taking into account the geometry and parameters of the HPGe crystal, design of the cryostat, source position and response of the detectors preamplifier. The only remaining free parameter was tuned to get agreement between measured and simulated pulses (“effective” temperature at which the charges were appropriately drifted). We have shown that the MC data can be successfully used to train the neural network. In the simulations we did not take into account slower pulses originating from the vicinity of the n^+ contact (Li drifted layer) [47,48]. They may be responsible for slight discrepancies between survival fractions obtained for the data and simulated pulses (Table 5).

For the presented prototype detector we plan to investigate performance of the ANN-based PSA on the removal of alpha induced events. This will be accomplished by exposing various detector parts (p^+ contact, passivation) to radon source in order to accumulate ^{210}Po . Bigger detectors, with masses up to 1.5 kg in the BEGe SAGE geometries, will be manufactured and tested as well.

Acknowledgements The technical support from Konrad Lojek (Jagiellonian University), Władysław Kowalski, Piotr Straczek and Mirosław Bartyzel (Institute of Nuclear Physics Polish Academy of Sciences) is acknowledged. We would also like to thank Yoann Kermaidic (Max-Planck-Institut für Kernphysik) and David Radford (Oak Ridge National Laboratory) for the help with the ADL and Siggen software packages. This work was supported by the Polish Ministry of Science and Higher Education (Grant no. DIR/WK/2018/08), Polish National Science Center (Grant no. UMO-2016/21/B/ST2/01094) and the Foundation for Polish Science (Grant No. POIR.04.04.00-00-2FFF/16).

Data Availability Statement This manuscript has no associated data or the data will not be deposited. [Authors' comment: The data used to generate results provided in the manuscript (especially the ones regarding the pulse shape analysis) is too large in size to be practically shared on-line.]

Open Access This article is licensed under a Creative Commons Attribution 4.0 International License, which permits use, sharing, adaptation, distribution and reproduction in any medium or format, as long as you give appropriate credit to the original author(s) and the source, provide a link to the Creative Commons licence, and indicate if changes

were made. The images or other third party material in this article are included in the article's Creative Commons licence, unless indicated otherwise in a credit line to the material. If material is not included in the article's Creative Commons licence and your intended use is not permitted by statutory regulation or exceeds the permitted use, you will need to obtain permission directly from the copyright holder. To view a copy of this licence, visit <http://creativecommons.org/licenses/by/4.0/>.

Funded by SCOAP³.

References

1. M. Goeppert-Mayer, Double beta-disintegration. *Phys. Rev.* **48**(6), 512 (1935)
2. W.H. Furry, On transition probabilities in double beta-disintegration. *Phys. Rev.* **56**(12), 1184 (1939)
3. K. Grotz, H.V. Klapdor, Predictions of 2ν and 0ν double beta decay rates for nuclei with $A \geq 70$. *Phys. Lett. B* **157**(4), 242–246 (1985)
4. S. Dell'Oro et al., Neutrinoless double beta decay: 2015 review. *Adv. High Energy Phys.* **2016** (2016)
5. H.V. Klapdor-Kleingrothaus et al. [HdM Collaboration], Latest results from the Heidelberg-Moscow double beta decay experiment. *Eur. Phys. J. A* **12**, 147–154 (2001)
6. C.E. Aalseth et al. [Igex Collaboration], The Igex ^{76}Ge neutrinoless double beta decay experiment: prospects for next generation experiments. *Phys. Rev. D* **65**, 092007 (2002)
7. K.H. Ackermann et al. [Gerda Collaboration], The Gerda experiment for the search of $0\nu\beta\beta$ decay in ^{76}Ge . *Eur. Phys. J. C* **73**, 2330 (2013)
8. M. Agostini et al. [Gerda Collaboration], Results on neutrinoless double- β Decay of ^{76}Ge from Phase I of the Gerda experiment. *Phys. Rev. Lett.* **111**, 122503 (2013)
9. H.V. Klapdor-Kleingrothaus et al., Search for neutrinoless double beta decay with enriched ^{76}Ge in Gran Sasso 1990–2003. *Phys. Lett. B* **586**, 198–212 (2004)
10. M. Agostini et al. [Gerda Collaboration], Upgrade for Phase II of the Gerda experiment. *Eur. Phys. J. C* **78**, 388 (2018)
11. M. Agostini et al., Background-free search for neutrinoless double- β decay of ^{76}Ge with Gerda. *Nature* **544**(7648), 47 (2017)
12. M. Agostini et al. [Gerda Collaboration], Improved limit on neutrinoless double- β decay of ^{76}Ge from from Gerda Phase II. *Phys. Rev. Lett.* **120**, 132503 (2018)
13. M. Agostini et al. [Gerda Collaboration], Probing Majorana neutrinos with double- β decay. *Science* (2019). <https://doi.org/10.1126/science.aav8613>
14. M. Agostini et al., Final results of GERDA on the search for neutrinoless double- β decay (2020). [arXiv:2009.06079v1](https://arxiv.org/abs/2009.06079v1) [nucl-ex]
15. N. Abgrall et al. [Legend Collaboration], The large enriched Germanium Experiment for Neutrinoless Double Beta Decay (LEGEND). *Book Ser. AIP Conf. Proc.* **1894**, 020027 (2017)
16. Y. Kermaidic, GERDA, MAJORANA and LEGEND – towards a background-free ton-scale ^{76}Ge experiment, Talk at Neutrino (2020). https://indico.fnal.gov/event/43209/contributions/187846/attachments/129106/159515/20200701_Nu2020_Ge76_YoannKermaidic.pdf
17. M. Agostini et al., Characterization of 30 ^{76}Ge enriched Broad Energy Ge detectors for GERDA Phase II. *Eur. Phys. J. C* **79**(11), 1–24 (2019)
18. D. Budjas et al., Pulse shape discrimination studies with a Broad-Energy Germanium detector for signal identification and background suppression in the Gerda double beta decay experiment. *J. Instrum.* **4**(10), P10007 (2009)
19. M. Agostini et al., Pulse shape discrimination for Gerda Phase I data. *Eur. Phys. J. C* **73**(10), 2583 (2013)
20. M. Misiaszek et al., Improving sensitivity of a BEGe-based high-purity germanium spectrometer through pulse shape analysis. *Eur. Phys. J. C* **78**(5), 392 (2018)
21. S.I. Alvis et al., Multisite event discrimination for the Majorana demonstrator. *Phys. Rev. C* **99**(6), 065501 (2019)
22. R.J. Cooper et al., A novel HPGe detector for gamma-ray tracking and imaging. *Nucl. Instrum. Methods Phys. Res. Sect. A Accel. Spectrom. Detect. Assoc. Equip.* **665**, 25–32 (2011)
23. A. Domula et al., Pulse shape discrimination performance of inverted coaxial Ge detectors. *Nucl. Instrum. Methods Phys. Res. Sect. A* **891**, 106 (2018)
24. W.L. Hansen, E.E. Haller, Fabrication techniques for reverse electrode coaxial germanium nuclear radiation detectors. *IEEE Trans. Nucl. Sci.* **28**(1), 541–543 (1981)
25. M. Wojcik, G. Zuzel, H. Simgen, Review of high-sensitivity Radon studies. *Int. J. Mod. Phys. A* **32**, 1743004 (2017)
26. A.S. Adekola et al., Performance of a small anode germanium well detector. *Nucl. Instrum. Methods Phys. Res. Sect. A Accel. Spectrom. Detect. Assoc. Equip.* **784**, 124–130 (2015)
27. P.S. Barbeau, J.I. Collar, O. Tench, Large-mass ultralow noise germanium detectors: performance and applications in neutrino and astroparticle physics. *J. Cosmol. Astropart. Phys.* **2007**(09), 009 (2007)
28. Umicore, supplier of High Purity Germanium crystals. <https://eom.umicore.com/en/germanium-solutions/products/high-purity-germanium-crystals/>
29. V.B. Brudanin et al., Large-volume HPGe detectors for rare events with a low deposited energy. *Instrum. Exp. Tech.* **54**(4), 470 (2011)
30. H. Herzer et al., Ion implanted high-purity germanium detectors. *Nucl. Instrum. Methods* **101**(1), 31–37 (1972)
31. Q. Looker, Fabrication process development for high-purity germanium radiation detectors with amorphous semiconductor contacts, Dissertation UC Berkeley (2014)
32. G. Maggioni et al., Characterization of different surface passivation routes applied to a planar HPGe detector. *Eur. Phys. J. A* **51**(11), 141 (2015)
33. Liner Systems, datasheet for 2N/PN/SST4391 series of single n-channel J-FET switches. http://www.linearsystems.com/lsdata/datasheets/2N4391_Low_Noise_N-Channel_JFET_Switch.pdf
34. E.W. Kühn, A.N.F. Schroeder, Capacitance measurement on biased Ge (Li) and Si (Li) radiation detectors used with cooled FET input. *Nucl. Instrum. Methods* **79**(2), 304–308 (1970)
35. M. Agostini et al., Improvement of the energy resolution via an optimized digital signal processing in GERDA Phase I. *Eur. Phys. J. C* **75**(6), 255 (2015)
36. G.F. Knoll, *Radiation Detection and Measurement* (Wiley, New York, 2010)
37. R.G. de Orduna et al., Pulse shape analysis for background reduction in BEGe detectors. EUR 24521EN, European Union (2010). <https://doi.org/10.1007/s10967-010-0729-8>
38. C.H.M. Broeders, A.Y. Konobeyev, Systematics of (p, n) reaction cross-section. *Radiochim. Acta* **96**(7), 387–397 (2008)
39. B. Bruyneel, B. Birkenbach, P. Reiter, Pulse shape analysis and position determination in segmented HPGe detectors: The AGATA detector library. *Eur. Phys. J. A* **52**(3), 70 (2016)
40. M. Agostini et al., Signal modeling of high-purity Ge detectors with a small read-out electrode and application to neutrinoless double beta decay search in Ge-76. *J. Instrum.* **6**(03), P03005 (2011)
41. A. Caldwell et al., Signal recognition efficiencies of artificial neural-network pulse-shape discrimination in HPGe $0\nu\beta\beta$ -decay searches. *Eur. Phys. J. C* **75**(7), 350 (2015)
42. O.A. Ponkratenko, V.I. Tretyak, Y.G. Zdesenko, Event generator DECAY4 for simulating double-beta processes and decays of radioactive nuclei. *Phys. At. Nuclei* **63**(7), 1282–1287 (2000)
43. D.C. Radford, Siggen/Fieldgen, Oak Ridge (2004). <http://radware.phy.ornl.gov/gretina/>

44. D. Palioselitis [GERDA collaboration], Experience from operating germanium detectors in GERDA. J. Phys. Conf. Ser. **606**(1) (2015)
45. M. Agostini et al., Characterization of a broad energy germanium detector and application to neutrinoless double beta decay search in ^{76}Ge . J. Instrum. **6**(04), P04005 (2011)
46. N. Abgrall et al., The Majorana Demonstrator neutrinoless double-beta decay experiment. Adv. High Energy Phys. **2014** (2014)
47. B. Lehnert, *Investigation of n+ surface events in HPGe detectors for liquid argon background rejection in GERDA* (Verh. der Dtsch. Phys. Ges, 2015)
48. B. Lehnert, Background rejection of n+ surface events in GERDA Phase II. J. Phys. Conf. Ser. **718**(6) (2016) (**IOP Publishing**)